

An Exploration of Soil Moisture Reconstruction Techniques

Spencer Nishimoto Low

A thesis submitted to the faculty of
Brigham Young University
in partial fulfillment of the requirements for the degree of
Master of Science

David G. Long, Chair
D.J. Lee
Cammy Peterson

Department of Electrical and Computer Engineering
Brigham Young University

Copyright © 2021 Spencer Nishimoto Low

All Rights Reserved

ABSTRACT

An Exploration of Soil Moisture Reconstruction Techniques

Spencer Nishimoto Low

Department of Electrical and Computer Engineering, BYU

Master of Science

Satellite radiometers are used to remotely measure properties of the Earth's surface. Radiometers enable wide spatial coverage and daily temporal coverage. Radiometer measurements are used in a wide array of applications, including freeze/thaw states inference, vegetation index calculations, rainfall estimation, and soil moisture estimation. Resolution enhancement of these radiometer measurements enable finer details to be resolved and improve our understanding of Earth.

The Soil Moisture Active Passive (SMAP) radiometer was launched in April 2014 with a goal to produce high resolution soil moisture estimates. However, due to hardware failure of the radar channels, prepared algorithms could no longer be used. Current algorithms utilize a narrow spatial and temporal overlap between the SMAP radiometer and the SENTINEL-1 radar to produce high resolution soil moisture estimates that are spatially and temporally limited. This thesis explores the use of resolution enhancing algorithms to produce high resolution soil moisture estimates without the spatial coverage limitations caused by using multiple sensors.

Two main approaches are considered: calculating the iterative update in brightness temperature and calculating the update in soil moisture. The best performing algorithm is the Soil Moisture Image Reconstruction (SMIR) algorithm that is a variation of the Radiometer form of the Scatterometer Image Reconstruction (rSIR) algorithm that has been adapted to operate in parameter space. This algorithm utilizes a novel soil moisture measurement response function (SMRF) in the reconstruction. It matches or exceeds the performance of other algorithms and allows for wide spatial coverage.

Keywords: scatterometer, radiometer, soil moisture, backscatter, radar cross section, brightness temperature

ACKNOWLEDGMENTS

I would like to acknowledge my wife and family for all their support, as well as Dr. Long and the MERS lab for helping me have a great graduate experience.

TABLE OF CONTENTS

LIST OF TABLES	vi
LIST OF FIGURES	vii
Chapter 1 Introduction	1
1.1 Radiometry	1
1.2 Soil Moisture Active Passive (SMAP) Mission	2
1.2.1 Soil Moisture Retrieval	3
1.3 Summary of Results	5
1.3.1 Thesis Organization	6
Chapter 2 Background	7
2.1 SMAP Mission	7
2.1.1 Introduction	7
2.1.2 Hardware	8
2.1.3 Data Product	10
2.1.4 SENTINEL-1 Radar	10
2.1.5 Disaggregation Algorithm	11
2.2 Algorithm Background	14
2.2.1 Soil Moisture Algorithm	14
2.2.2 rSIR	17
2.3 rSIR Integration	23
Chapter 3 Algorithm Overview and Simulations	24
3.1 Non-Linear Characteristics of the rSIR and Soil Moisture Algorithm	24
3.2 Sequential rSIR Soil Moisture Algorithm	25
3.3 Soil Moisture form of rSIR	25
3.4 Soil Moisture Image Reconstruction	26
3.5 Simulations	26
3.5.1 SMrSIR Simulation	29
3.5.2 SMIR Simulation	30
3.5.3 Simulation Results	31
Chapter 4 rSIR Updates using Brightness Temperature Measurements	36
4.1 SMrSIR	36
4.1.1 Reverse Soil Moisture Transformation	36
4.2 SMrSIR Results	38
4.2.1 Area of Study	38
4.2.2 Results	39
4.3 Analysis	39

Chapter 5	rSIR Updates Using Soil Moisture Measurements	41
5.1	Update in Soil Moisture Space	41
5.1.1	Soil Moisture Measurements	42
5.1.2	Soil Moisture Update, using T_B Measurement Response Function	44
5.1.3	Soil Moisture Response Function Approach	46
5.1.4	Soil Moisture Footprint Derivation	46
5.1.5	SMRF Corrections	54
5.2	Analysis	60
Chapter 6	Conclusion	67
6.1	Contributions	68
6.2	Future Work	69
REFERENCES		70

LIST OF TABLES

3.1	Summary of simulation errors for the various different methods after 50 rSIR iterations.	32
5.1	Table of errors that have been averaged over a 7-day window.	64

LIST OF FIGURES

1.1	A 3D rendering of the SMAP sensor in orbit. The antenna reflector (on top) spins at 18 RPM, covering a wide swath [1].	3
1.2	One day global SMAP brightness temperature (T_B) image. Data is from day 276 of 2016.	4
1.3	One day global soil moisture image produced using data from SMAP and SENTINEL-1. Data is from day 276 of 2016. There is a significant reduction in spatial coverage compared to the SMAP global T_B image in Fig. 1.2.	5
1.4	An example of a 10-day SMAP/SENTINEL-1 soil moisture image. This image is of soil moisture content of North America. This image is produced using day 276 to 286 of 2016. The blue streaks are areas with missing or corrupted data.	6
2.1	Illustration of the SMAP instrument. This figure was taken from [1].	8
2.2	Illustration showing the SMAP radiometer geometry and swath [1].	9
2.3	Image of overlapping SENTINEL-1 and SMAP coverage for one day. Only measurements with a similiar LTOD are used. This image shows measurements for day 276 of 2016. The values are roughness values derived from backscatter measurements. This shows the relatively little overlap for any given day. The much narrower swath is also visible [2].	11
2.4	Plot showing SMAP v-pol brightness temperature values plotted against QuikSCAT Ku-band backscatter values for a given NDVI range. In this plot $0.3 < NDVI < 0.4$. There is very little correlation between the two values. The data is from day 276 of 2014.	13
2.5	An example image of the MRF used. This is taken from day 276 of 2016.	18
2.6	A surface plot of an example SMAP MRF used.	19
2.7	rSIR image made using SMAP data from day 276 of 2016. This is made using a 3-km pixel size. The effective resolution is coarser than the pixel size. This image is zoomed in over the mouth of the Amazon river to show various details in the image.	21
2.8	rSIR image made using SMAP data from day 276 of 2016. This is made using a 9-km pixels size. This image is zoomed in over the mouth of the Amazon river to show various details in the image. There is an increase in pixelization on the borders of the river.	22
2.9	Drop-in-the-bucket gridded image made using SMAP data from day 276 of 2016. This is made using a 36-km pixels size. This image is zoomed in over the mouth of the Amazon river to show various details in the image. In this case, there is extreme pixelization. This pixel size corresponds with the radiometer footprint size.	23
3.1	Flowchart of the sequential rSIR soil moisture algorithm.	25
3.2	Flowchart of the SMrSIR algorithm approach.	26
3.3	Flowchart of the SMIR algorithm.	27
3.4	Brightness temperature truth image for simulations. Radiometer measurements are simulated by sampling this image according to the SMAP geometry.	28
3.5	Soil moisture truth image produced using the simplified soil moisture transformation. Radiometer measurements in Eq. 2.16 are simulated by sampling the brightness temperature in Fig. 3.4.	29

3.6	Example of a simulation MRF. This MRF is similar to a typical MRF used by the SMAP sensor.	30
3.7	Simulation results for the sequential rSIR soil moisture algorithm.	31
3.8	Soil moisture result of the combined rSIR algorithm using a brightness temperature update after 50 iterations using the simplified soil moisture algorithm described in Eq. 3.2.	32
3.9	Percent error between the SMrSIR output and the truth image for the simulation.	33
3.10	Result of a combined rSIR algorithm using a soil moisture update after 50 iterations.	34
3.11	Percent error between the SMIR output and the truth image for the simulation.	35
4.1	Global image with a bounding box around the area of study. This area is chosen because it has a wide range of soil moisture values and many features that are resolved. This image is made using data from day 276 of 2016.	38
4.2	Figure showing the results of the combined rSIR and soil moisture algorithm. This data is taken from day 276 of 2016. This figure shows some of the quantization error. Fig. 4.1 shows the area of study in this thesis. This sub-image is approximately 900 by 900 kilometers.	40
5.1	A SMAP-SENTINEL-1 soil moisture estimate produced by the SMAP team at the NSIDC. This sample corresponds with the data used in this chapter, sharing the same coverage and time. This data is from the 276 day of 2016. This image is made using 3 km pixels [2].	42
5.2	Results from the sequential algorithm. This image is made using data from day 276 of 2016.	43
5.3	The AVE image produced using the soil moisture measurements and the brightness temperature MRF. This 3-km pixel image is made using data from day 276 of 2016.	44
5.4	The soil moisture output of the SMIR algorithm using the T_B MRF after fifteen iterations. Comparing the results of the AVE iteration of SMIR using the T_B MRF, and the output after 15 iterations. In both images we can see a general loss in detail, and artifacts from the MRF appearing. This is likely due to the brightness temperature MRF being incompatible with the soil moisture measurements.	45
5.5	Collection of figures showing the ancillary data for the region of interest. This collection reveals where the details in the soil moisture estimate come from. This data comes from day 276 of 2016.	47
5.6	Example of a non-zero mean SMRF. The features are same as the zero mean SMRF. The main difference is the range of values. This particular SMRF is made over northern China using data from day 276 of 2016. The fine grained details in the SMRF arise from the fine details in the ancillary data. Each SMRF differs each other as the features in each footprint are different.	49
5.7	AVE image made using the non-zero SMRF. Note the general lack of detail, and features in the image. This image is produced using data from day 276 of 2016.	50
5.8	Example of a zero-mean SMRF made over Northern China. Made using data from day 276 of 2016. The fine grained details in the SMRF arise from the fine details in the ancillary data. Each SMRF differs each other as the features in each footprint are different.	51

5.9	Surface plot of a zero mean SMRF. This figure shows the high resolution details as well as missing data pixels. The missing data pixels are caused by data missing in the ancillary data.	52
5.10	AVE image created using the zero mean SMRF. This image is centered over the Amazon river. Note the increase in detail and features in the image but also the negative values. Data is from day 276 of 2016.	53
5.11	A corrected AVE image produced by taking the absolute value of the zero mean AVE image shown in Fig. 5.10. This image is made using data from day 276 of 2016.	54
5.12	Example of features and details present in SMIR soil moisture estimate, but not present in the SENTINEL-1 soil moisture estimate. Compare with Fig. 5.13	55
5.13	Example of features and details present in SMIR soil moisture estimate, but not present in the SENTINEL-1 soil moisture estimate. Compare with Fig. 5.12	56
5.14	Absolute value of an example SMRF. This is made using the same data as in Fig. 5.9	57
5.15	Resulting AVE image using the absolute value of the SMRF. It is important to note the general loss in detail in the image. Made using data from day 276 of 2016.	58
5.16	Result of the absolute value SMRF after fifteen iterations of the combined rSIR algorithm. Made using data from day 276 of 2016.	59
5.17	Soil moisture estimate from day 280 of 2016. This image is made using the $SMRF_{abs}$. This image is taken from the same area of study as outlined in Fig 4.1	60
5.18	A more centered view of the area from Fig 5.17. This is again data from day 280 of 2016. When compared with Fig 5.19, we can see that much of the details and features are present.	61
5.19	A soil moisture estimate produced by JPL using SMAP and SENTINEL-1 measurements. This is made using data from day 280. This view is identical to that of Fig. 5.18 for comparison.	62
5.20	AVE image produces using the inverse of the SMRF. This AVE image retains much more detail compared to the other methods proposed.	63
5.21	SIR image produced after fifteen iterations using the inverse of the SMRF.	64
5.22	Average produced using the Negative Lobe of the SMRF. This image is made using data from day 276 of 2016.	65
5.23	SMIR image produced after 15 iterations using the negative lobe of the SMRF. This image is produced using data from day 276 of 2016.	66

CHAPTER 1. INTRODUCTION

Spaceborne remote sensors are able to measure the Earth's surface with wide spatial and temporal coverage, enabling researchers to better study the complex cycles that exist on Earth. These include the water, energy, and carbon cycles, soil moisture, wind currents, ocean currents, ice melts, and sea ice growth [3], [4], [5]. Radiometry is used to measure emitted electromagnetic waves from the Earth's surface [6]. Algorithms use radiometer measurements to infer a great deal of information about the conditions of the surface. The Soil Moisture Active Passive (SMAP) mission by JPL is designed to measure soil moisture [7]. Originally, SMAP included a radar and radiometer, but the radar suffered hardware failure early in its mission [8]. This failure prevents the creation of high resolution soil moisture data products using existing algorithms. To overcome this limitation, this thesis explores the use of variations of the Radiometer form of the Scatterometer Image Reconstruction (rSIR) algorithm to produce a finer resolution soil moisture data product. Specifically, this thesis combines the rSIR algorithm with the soil moisture algorithm into one soil moisture image reconstruction algorithm that is able to produce high resolution, accurate soil moisture images. Two main approaches are considered: calculating the iterative update in brightness temperature, and calculating the update in soil moisture.

1.1 Radiometry

Radiometry is based on measuring the blackbody or Planck's radiation emitted by an object [9]. Because radiometers do not actively transmit any energy they are considered passive sensors. In this thesis, radiometry is used from spaceborne satellites to measure the emitted radiation from the Earth's surface. This measurement is termed brightness temperature (T_B). Brightness temperature is defined as a function of the surface temperature

$$T_B = \epsilon T_P \tag{1.1}$$

where ε is the emissivity of the surface and T_P is the physical temperature of the surface [6]. In most cases ε is the variable of interest. By knowing the surface temperature, one can solve for ε

$$\varepsilon = \frac{T_B}{T_P}. \quad (1.2)$$

The surface emissivity provides a great deal of information about the surface. With soils, this value can be used to determine the mixture of clay, loam, silt, and water [6]. This is later exploited in soil moisture calculations to determine how much water is present in soil.

1.2 Soil Moisture Active Passive (SMAP) Mission

The SMAP mission, launched in April of 2015, is designed to allow for the study of the surface soil moisture. The sensor reports the percentage of the soil volume that is water in each pixel over a wide swath. The SMAP instrument (Fig. 1.1) design is uniquely tailored to this goal [1]. The instrument houses both an L-band passive radiometer and an L-band active radar. By fusing information from both sensors, high resolution soil moisture images are produced. However, early in the mission the active radar experienced a power supply failure resulting in a loss of the active radar [8]. This degrades the resolution of the soil estimate. To solve this issue, new digital signal processing techniques are developed to again produce high resolution soil moisture images [10].

In order to continue the SMAP mission, JPL developed new algorithms to estimate soil moisture. The algorithm currently employed by JPL uses active radar measurements from the SENTINEL-1 mission as an alternative for the non-functional SMAP radar [4]. Using the SENTINEL-1 radar provides the needed information for their pre-existing algorithms at the cost of spatial coverage. This is due to both the orbit and narrow swath of SENTINEL-1. The new algorithms explored in this thesis do not require active radar measurements, thereby gaining the ability to produce estimates with a greater spatial coverage. The stark difference between the spatial coverage can be seen in Fig. 1.2 and 1.3. Fig. 1.4 shows how limiting the spatial coverage of the SENTINEL-1 algorithm is. Even after using ten days of data, a complete image of the continental United States cannot be made.

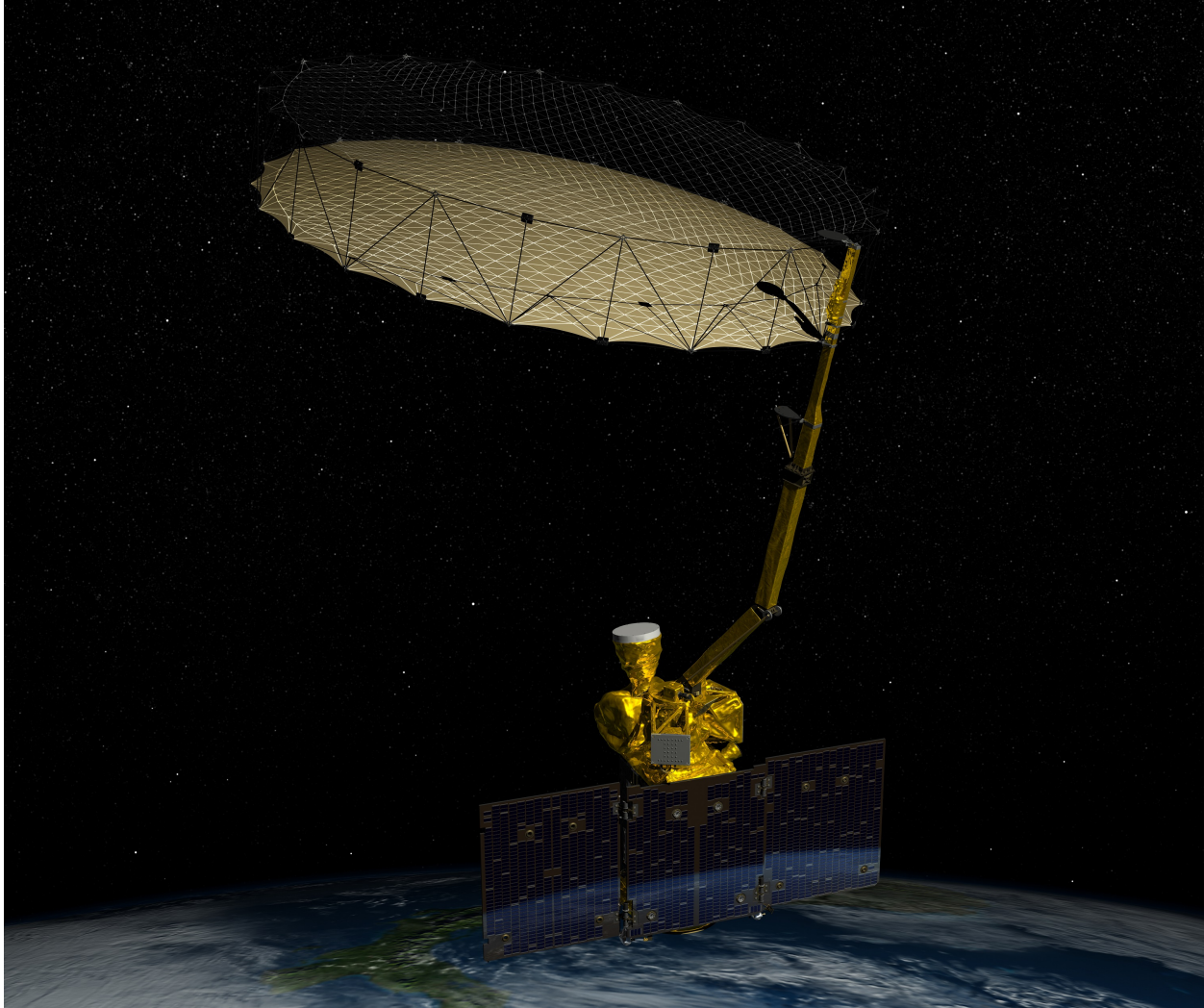


Figure 1.1: A 3D rendering of the SMAP sensor in orbit. The antenna reflector (on top) spins at 18 RPM, covering a wide swath [1].

1.2.1 Soil Moisture Retrieval

The soil moisture algorithm requires brightness temperature measurements and collections of ancillary data. The collections of ancillary data have finer resolutions than that of the degraded brightness temperature measurements. The resolution of the soil moisture images is, therefore, limited by the resolution of the brightness temperature measurements. Current algorithms address this by using high resolution reconstruction algorithms to increase the resolution of the brightness temperature measurements [10]. This in turn, results in an improvement to the soil moisture estimate resolution.

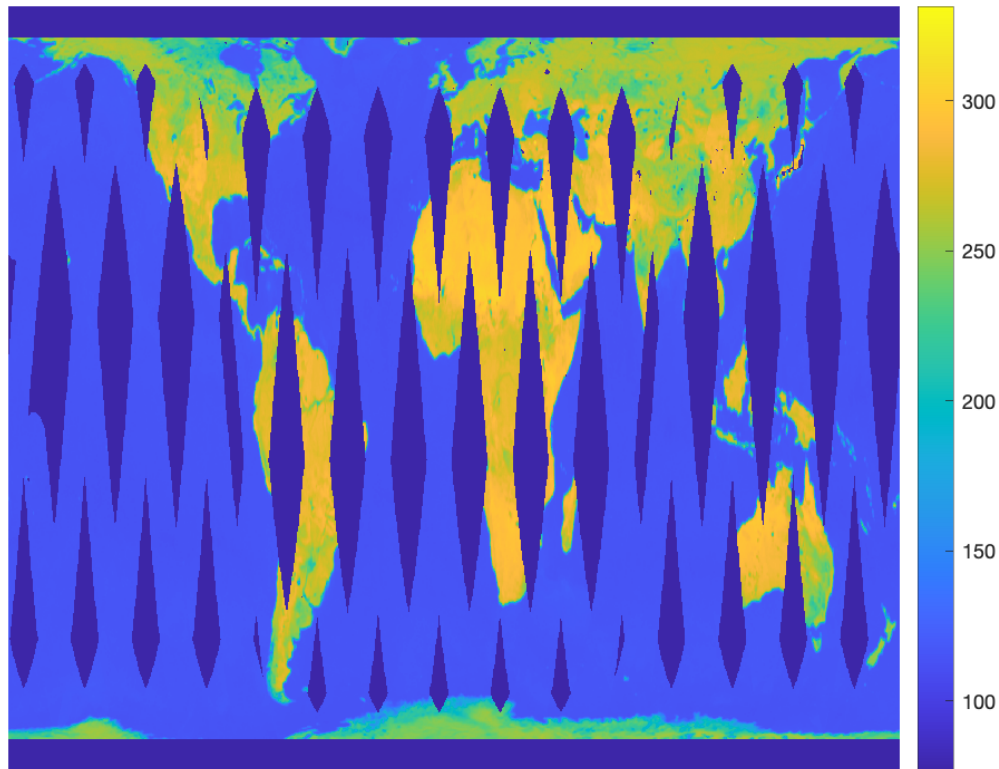


Figure 1.2: One day global SMAP brightness temperature (T_B) image. Data is from day 276 of 2016.

In this thesis, I examine another approach to producing finer resolution soil moisture estimates. Rather than increase the brightness temperature measurements prior to the soil moisture conversion, I apply resolution enhancement algorithms to low resolution soil moisture estimates. Due to the non-linear nature of both the reconstruction and soil moisture algorithms, this change produces different results. This thesis derives and tests variations of the rSIR algorithm, which utilizes information about the antenna gain pattern to produce higher resolution brightness temperature images. Currently this algorithm has been tested on multiple active and passive sensors and their raw measurements. It has not previously been adapted to operate on transformed measurements and parameter estimation.

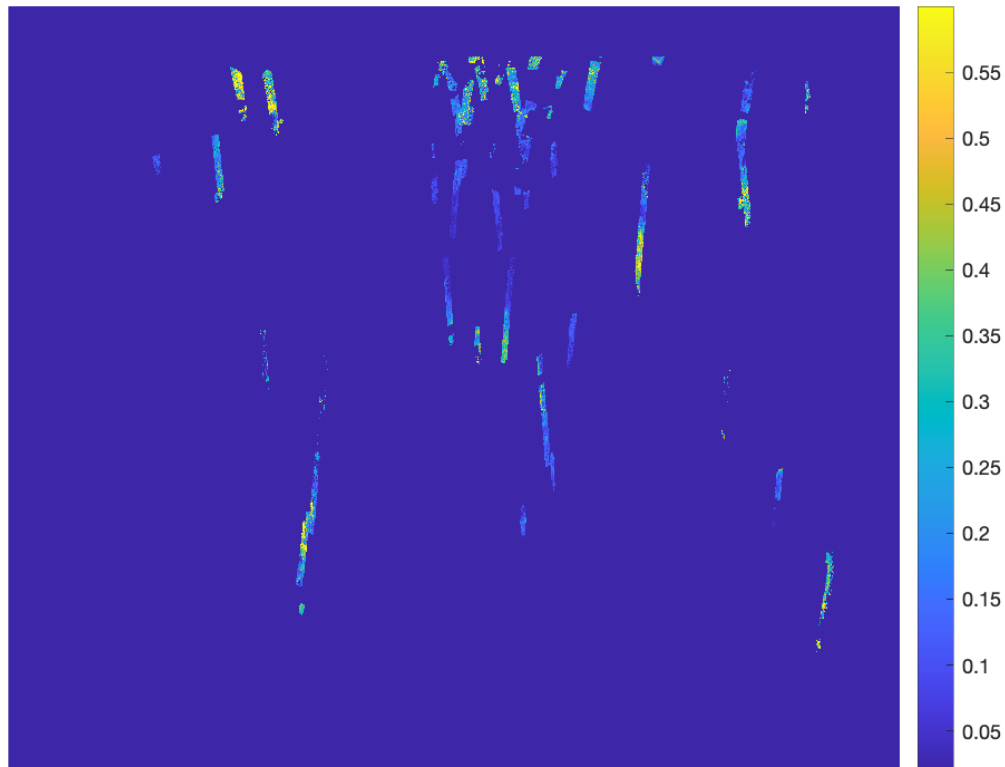


Figure 1.3: One day global soil moisture image produced using data from SMAP and SENTINEL-1. Data is from day 276 of 2016. There is a significant reduction in spatial coverage compared to the SMAP global T_B image in Fig. 1.2.

1.3 Summary of Results

Employing a combination of the rSIR and soil moisture algorithms that utilizes a soil moisture response function is found to produce the most detailed image. It does not perfectly match the soil moisture estimates produced using the SENTINEL-1 radar. Even so, while this method returns a small error when compared to the soil moisture estimates provided by JPL, this method does not require active radar measurements in order to up-sample the brightness temperature images. Ultimately this means the combined algorithm can be used on the full SMAP swath as compared to the small area of overlap between the SMAP and SENTINEL-1 swath. This method provides finer resolution at the cost of accuracy.

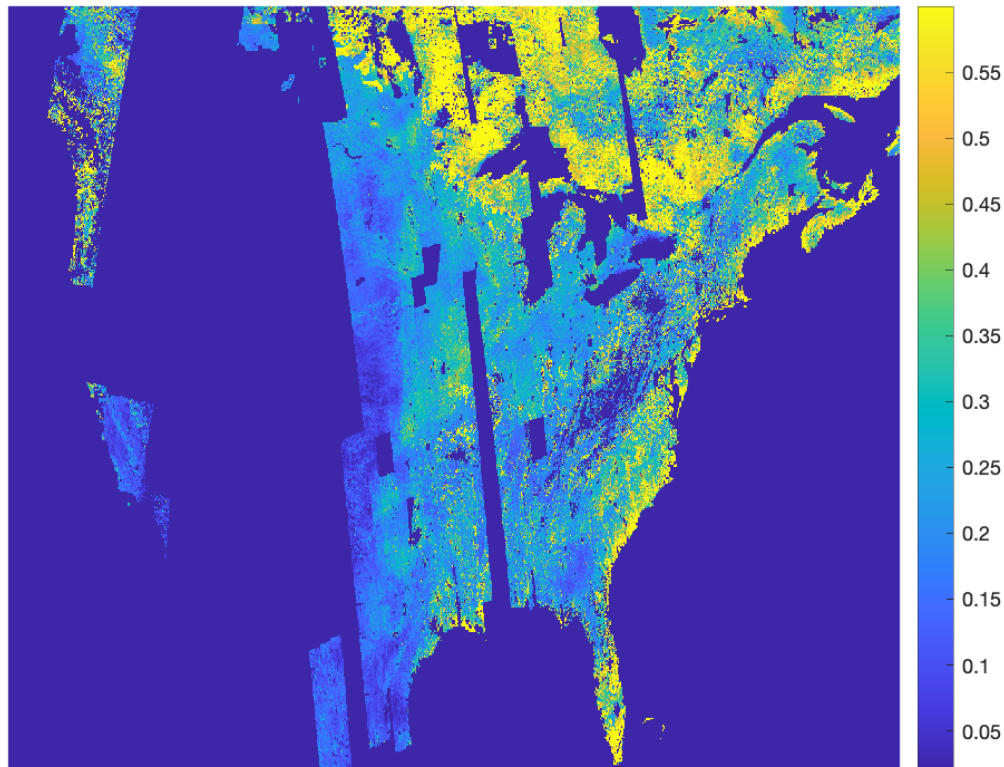


Figure 1.4: An example of a 10-day SMAP/SENTINEL-1 soil moisture image. This image is of soil moisture content of North America. This image is produced using day 276 to 286 of 2016. The blue streaks are areas with missing or corrupted data.

1.3.1 Thesis Organization

Chapter 2 provides a detailed background, discusses the instrument in greater detail, and provides a background of the soil moisture algorithm and the rSIR algorithm. Chapter 3 provides an overview of the new algorithms and discusses the simulations run. Chapter 4 derives the combined rSIR-soil-moisture algorithm where the update is calculated in brightness temperature. Chapter 5 derives two versions of the combined rSIR-soil-moisture algorithm where the update is calculated in soil moisture. Chapter 6 discusses the conclusions drawn from this exploration.

CHAPTER 2. BACKGROUND

Satellite based radiometer soil moisture measurements are found using a combination of in-situ information and brightness temperature measurements. These soil moisture measurements are rasterized into images, where the resolution is determined by the spatial resolution of individual brightness temperature measurements. High resolution brightness temperature reconstruction produces images where the pixel size is smaller than the radiometer footprint [11]. For the SMAP sensor, the footprint is approximately 36 kilometers in diameter [4]. The target resolution for the soil moisture measurements is 3 kilometer pixels. Various algorithms have been created to produce high resolution soil moisture estimates, each with its own set of trade offs. Originally, the SMAP sensor included a high resolution co-located radar that provided the additional information required to produce high resolution brightness temperature measurements. However, due to a power supply failure, the radar is no longer functional, and new methods to achieve the mission's goals are required [8]. This thesis explores the rSIR algorithm, a non-linear, iterative reconstruction approach as a new method to produce high resolution soil moisture estimates.

2.1 SMAP Mission

2.1.1 Introduction

NASA's Soil Moisture Active Passive (SMAP) satellite was launched in January of 2015. This mission focuses on remotely measuring soil moisture of the Earth's surface. The satellite carries an L-band radar and L-band radiometer. This unique configuration enables concurrent measurements and combines the strengths of both radar and radiometer systems. The scientific objectives of this mission are to [12]:

- Better understand the processes that link the terrestrial water, energy, and carbon cycles.
- Estimate global water and energy fluxes at the land surface.

- Quantify net carbon flux in boreal landscapes.
- Enhance weather and climate forecast ability.
- Develop improved flood prediction and drought monitoring capability.

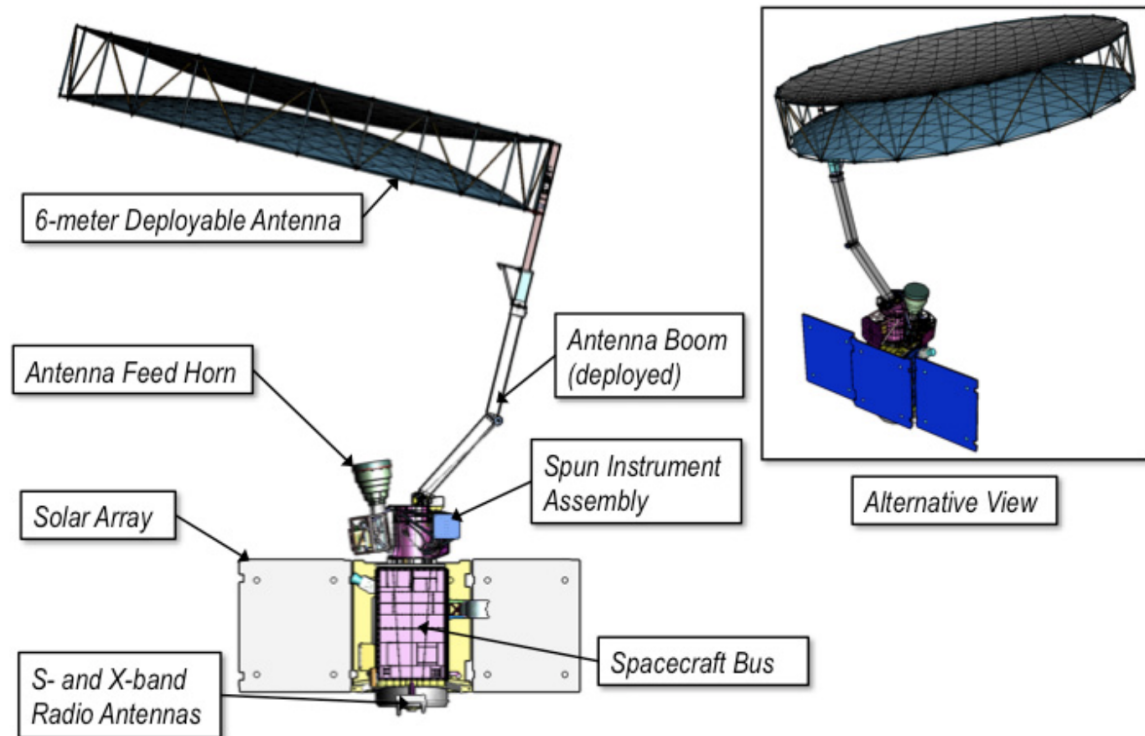


Figure 2.1: Illustration of the SMAP instrument. This figure was taken from [1].

2.1.2 Hardware

The SMAP instrument (Fig. 2.1) is unique in that it includes both an L-band radar and L-band radiometer. The two instruments are co-located using a 6 meter aperture reflector antenna that scans the Earth. The SMAP instrument measures a 1,000 km wide swath from an orbital altitude of 685 km. It uses a conically scanning antenna beam created by the rotating reflector dish that spins at 14.6 rpm. Fig. 2.2 illustrates this geometry.

Radiometer

The polarimetric radiometer measures the brightness temperature at the Earth's surface at the horizontal and vertical polarizations as well as the third and fourth Stokes parameters. The radiometer is connected to a rotating reflector that rotates between 13 and 14.6 rpm. This produces a canonically scanning beam with a 40-km, 3db footprint. The radiometer scans the surface at an approximately constant 40 degree incidence angle. The polarimetric radiometer has a 40 km spatial resolution and the dual-polarized radar has a 3 km spatial resolution. The radiometer operates in the L-band at 1.4135 GHz with a bandwidth of 24 MHz. The rotating beam affects the measurement response functions that are discussed later [13]. It has a 3-day revisit time for soil moisture measurements, with a 2-day revisit time at the higher latitudes.

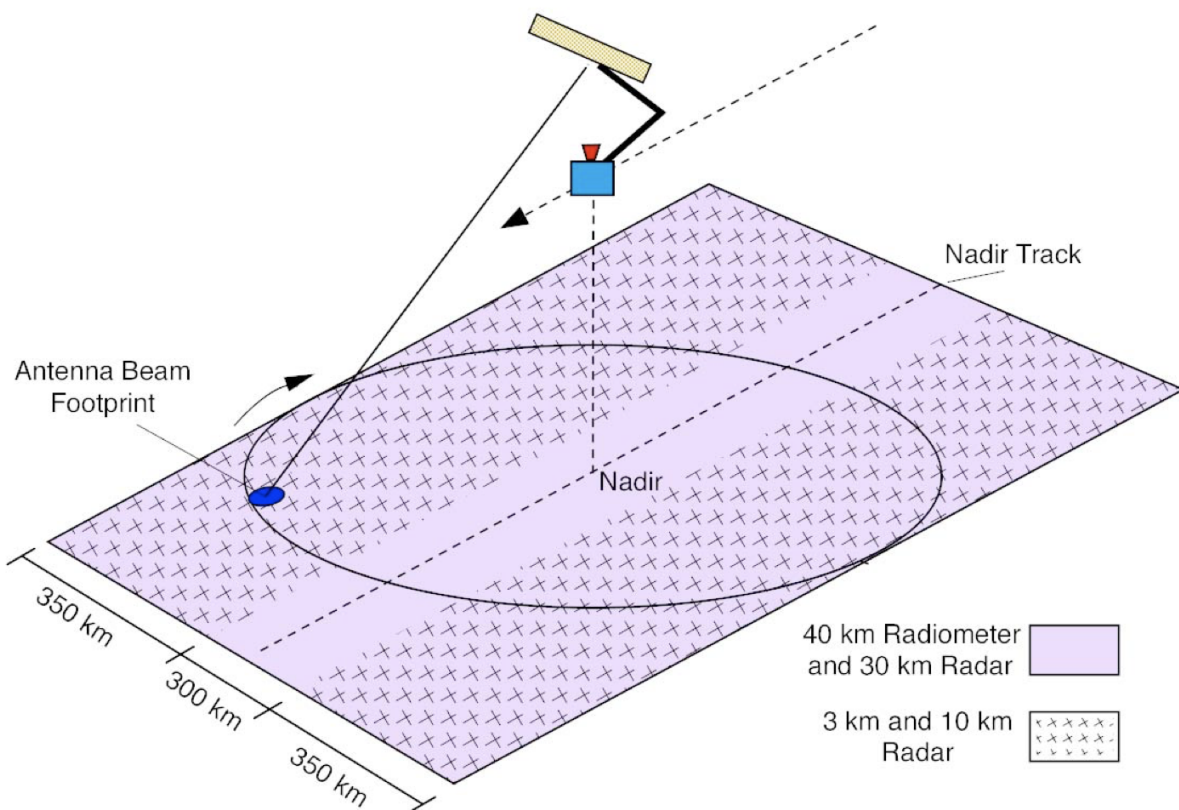


Figure 2.2: Illustration showing the SMAP radiometer geometry and swath [1].

Radar

The active radar measured the backscatter cross section of the Earth's surface at both the HH and VV co-polarizations, as well as the cross polarizations, HV and VH. The active radar had a 3-km resolution over 70% of the 1000-km swath [1]. The active radar experienced a power system failure early in the mission's life, resulting in a loss of the active radar. It is not considered further in this thesis.

2.1.3 Data Product

The SMAP mission provides multiple levels of data products for researchers. The data products include various brightness temperature measurements at various levels of processing. These include raw measurements, swath based measurements, gridded estimates, and processed information such as soil moisture and freeze/thaw states. The finest resolution of these data products is 9 km pixels where the coarsest resolution is 36 km pixels, which corresponds with the radiometer footprint size [14].

2.1.4 SENTINEL-1 Radar

The JPL approach to overcome the hardware failure of the active radar system is to use radar data from the SENTINEL-1 mission to replace the SMAP radar in Eq. 2.1 [7]. SENTINEL-1 is a satellite SAR, with a sun synchronous, near polar, circular orbit that resembles the SMAP orbit. The spacecraft orbits at a height of 693 kilometers and has a twelve day repeat cycle. The spacecraft carries a C-SAR instrument, which is centered at 5.405 GHz. This C-band radar has little atmospheric interference and has a clear view of the Earth's surface [15]. While this frequency does not match that of the SMAP radar, it is close enough to be used to infer surface roughness.

The SENTINEL-1 orbit resembles the SMAP orbit and enables synchronous LTOD measurements. The synchronous measurements between the SMAP radiometer and SENTINEL-1 radar have consistent correlation. This is crucial for the β term calculation in the disaggregation algorithm. However, the swath of SENTINEL-1 is much narrower. This results in relatively little spatial coverage due to limited overlap between the two sensors (Fig. 2.3). Despite this limited coverage, SENTINEL-1 measurements are the finest resolution replacement for the SMAP radar

measurements. The new algorithms discussed in this thesis are not limited to the narrow overlap between SMAP and other sensors. This enables high resolution soil moisture estimates to be made over the entire SMAP swath.

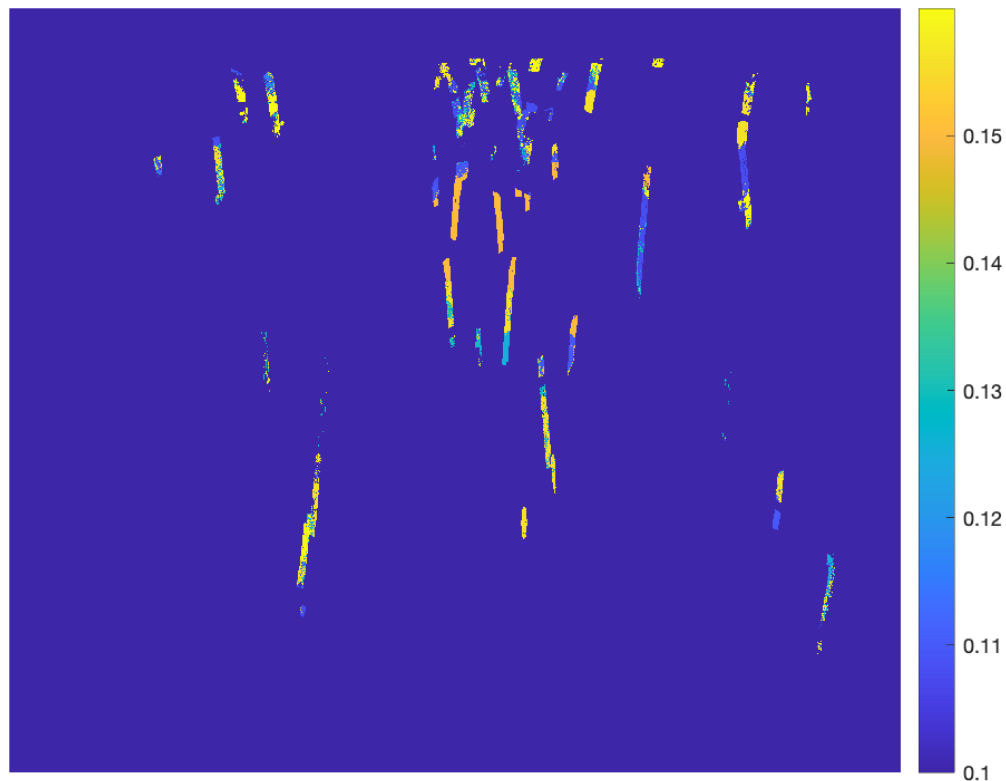


Figure 2.3: Image of overlapping SENTINEL-1 and SMAP coverage for one day. Only measurements with a similar LTOD are used. This image shows measurements for day 276 of 2016. The values are roughness values derived from backscatter measurements. This shows the relatively little overlap for any given day. The much narrower swath is also visible [2].

2.1.5 Disaggregation Algorithm

Before the radar failure, the measurements from the active radar and passive radiometer were combined using a disaggregation method to produce high-resolution, 9-km soil moisture

measurements [16]. The disaggregation equations for the corrected measurements are

$$T_{BP}(M_j) = T_{BP}(C) + \beta(C) * [\sigma_{pp}(M_j) - \sigma_{pp}(C)] + \Gamma * [\sigma_{pq}(C) - \sigma_{pq}(M_j)] \quad (2.1)$$

$$\Gamma = \left[\frac{\delta \sigma_{pp}(M_j)}{\delta \sigma_{pq}(M_j)} \right], \quad (2.2)$$

$$\sigma_{pp}(M_j) = \sum_i^{nm_j} \sigma_{pp}(F_i) \quad (2.3)$$

where σ_{pp} is the p-polarization backscatter measurement, and β is a parameter relating T_B and σ . “M” represents measurements on the 9-km grid, “F” represents measurements on the 3-km grid, and the “C” represents the measurements on the 40-km grid at pixel j. β is found on a pixel-by-pixel basis. It is calculated as the slope of a temporal collection of backscatter cross-section measurements and brightness temperature measurements. Eq. 2.3 is a simple down-sampling equation that averages the finer resolution pixels into larger pixels.

Initially, I hypothesized that this disaggregation algorithm could be adapted to use radars other than the SMAP or SENTINEL-1 radars. If other radars could be used in the disaggregation algorithm, soil moisture estimates with greater spatial coverage could be produced. I used radar measurements collected by the QuikSCAT scatterometer as a substitute for the SMAP radar. QuikSCAT is chosen due to its somewhat similar sun synchronous orbit and wide swath. My analysis is based on the assumption that the surface roughness is temporally stationary between QuikSCAT radar and SMAP radiometer measurements. Using the normalized difference vegetation index (NDVI) only pixels with similar amounts of vegetation are compared [17]. However, upon experimentation, I found that there is very little correlation between the QuikSCAT roughness measurements and the SMAP radiometer. Fig. 2.4 illustrates the correlation analysis. This is determined through calculating the two dimensional correlation between the radar and radiometer.

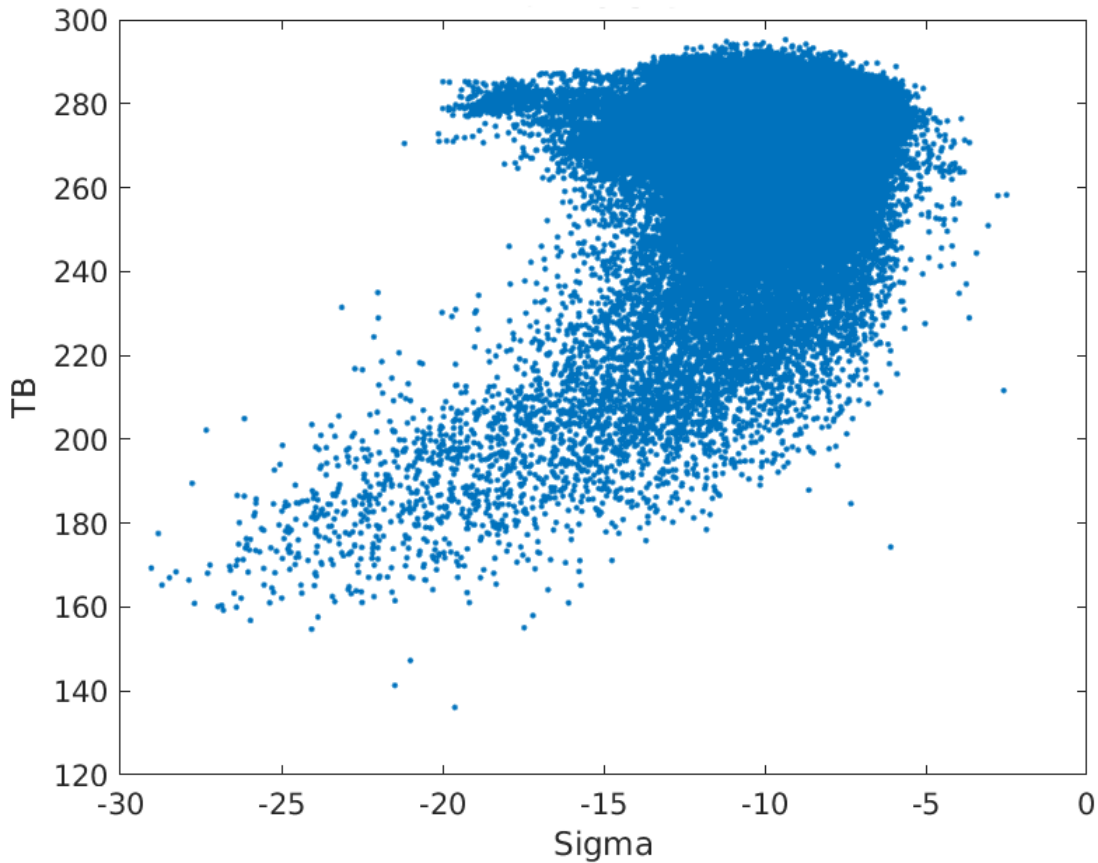


Figure 2.4: Plot showing SMAP v-pol brightness temperature values plotted against QuikSCAT Ku-band backscatter values for a given NDVI range. In this plot $0.3 < \text{NDVI} < 0.4$. There is very little correlation between the two values. The data is from day 276 of 2014.

This experiment was repeated using various other sensors such as the AQUA-AMSRE radiometer. I found limited correlation. This analysis is similar to the analysis performed by JPL when selecting SENTINEL-1 as a replacement radar. This leads me to the conclusion that the SENTINEL-1 is the most suitable radar replacement due to the small difference in the local time of day (LTOD) between the SMAP and SENTINEL-1 measurements [7]. This is due to the sensitivity of the disaggregation algorithm to temporal differences between the active and passive measurements. The SENTINEL-1 sensor operates in C-band which is close to the L-band that the SMAP radar operated at. Based on these findings, I determined that a different approach is required to produce high resolution soil moisture images. This led to the development of the combined soil moisture rSIR algorithm.

2.2 Algorithm Background

One approach to soil moisture resolution enhancement is to use the rSIR algorithm. The rSIR algorithm is used to enhance the resolution of SMAP brightness temperature measurements, which are in turn used to produce high resolution soil moisture estimates [10]. Current soil moisture estimation techniques separately utilize the soil moisture algorithm and the rSIR reconstruction technique. The brightness temperature images are first reconstructed using the rSIR algorithm, which are then input into the soil moisture algorithm. This method works but fails to capture all of the high resolution detail that could possibly be resolved. I postulate that better images may be reconstructed by combining both algorithms into a single high resolution soil moisture reconstruction algorithm.

It is expected that utilizing rSIR in conjunction with the soil moisture algorithm will produce high resolution images that are more accurate than the current approach produces. It is also expected that the different approaches will have slightly different resulting products due to their non-linearity. Before these new approaches are discussed further in later chapters, background descriptions of rSIR and the soil moisture algorithm are provided.

2.2.1 Soil Moisture Algorithm

The soil moisture algorithm uses a collection of ancillary data along with brightness temperature and backscatter measurements to estimate soil moisture. In this section, the dielectric mixing model and the forward soil moisture transformation are presented. The forward transformation is used in the soil moisture reconstruction techniques that are presented in later chapters. In Chapter 4 the reverse soil moisture transformation is derived. This background is beneficial in understanding that derivation as well.

Dielectric Mixing Model

The dielectric mixing model is used to find the soil dielectric constant. This model uses both the soil clay fraction provided in ancillary data sets and a range possible soil moisture estimates to calculate a range of possible dielectrics. This model is used in both the forward and

reverse transformation. The dielectric constant of the soil can be represented as a mixture of various different dielectrics. Using the soil clay fraction, this model is able to describe how much of various dielectrics there are in the soil and reports back an average [18].

Dielectric models of a solid mixed with water treat the water as discrete particles dispersed throughout the solid. The water is treated as either spherical or cylindrical particles depending on the model. Vegetation proves to be more difficult as the water is distributed continuously throughout a leaf or plant. [6] developed a linear model for the dielectric constant in vegetation

$$\epsilon_v = \epsilon_r + v_{fw}\epsilon_w + v_{bw}\epsilon_b, \quad (2.4)$$

where ϵ_r is the nondispersive residual component, ϵ_w and ϵ_b are the complex dielectric constants of free water and bound water, v_{fw} is the volume of fraction of free water, and v_{bw} is the volume fraction of bound water. The dielectric constants are found empirically. This in turn enables Eq. 2.4 to be exploited to find the free water and bound water volume fraction. This enables corrections to be made for vegetation water content and accurate calculation of water content in the soil.

Forward Soil Moisture Transformation

The forward transformation of brightness temperature measurements into soil moisture measurements is well documented [19]. This section provides a review of this algorithm. An understanding of the forward transformation is required to more fully understand the reverse soil moisture transformation.

The soil moisture transformation requires ancillary data in addition to brightness temperature measurements. This ancillary data includes:

- Surface Temperature
- Vegetation Water Content
- Scattering Albedo
- Vegetation Opacity
- Soil Roughness

- Soil Clay Fraction
- Waterbody Fraction

The soil moisture algorithm only considers pixels that have all the required ancillary data and T_B . The emissivity is calculated

$$\epsilon_{T_B} = \frac{T_B}{T_P}, \quad (2.5)$$

where ϵ_{T_B} is the emissivity, T_B is the brightness temperature and T_P is the physical surface temperature. The canopy transmissivity is calculated

$$T_C = e^{-\tau}, \quad (2.6)$$

where the canopy transmissivity is T_C , and vegetation opacity is τ . The emissivity is corrected for vegetation effects using the formula

$$\epsilon_{T_B} = \frac{\epsilon_{T_B} - 1 + T_C^2 + \alpha + \alpha T_C^2}{T_C^2 + \alpha T_C - \alpha * T_C^2}, \quad (2.7)$$

where the albedo is α . The emissivity is further corrected for surface roughness effects

$$\epsilon_{T_B} = 1 - (1 - \epsilon_{T_B}) e^{h \cos^2 \theta_i} \quad (2.8)$$

where h is the surface roughness and θ_i is the incidence angle. This emissivity constant is the corrected estimation that is found using the brightness temperature measurements.

Using the dielectric mixing model, a range of possible emissivity constants are calculated. First, the dielectric mixing model is used to calculate a range of dielectric constants that correspond to a range of possible soil moisture estimates. This range begins at 0% soil moisture and increments uniformly to 60% soil moisture. Then possible emissivity constants are calculated. Using Fresnel's equations

$$\epsilon_{PosH} = 1 - \left| \frac{\cos \theta_i - \sqrt{\kappa - \sin^2 \theta_i}}{\cos \theta_i + \sqrt{\kappa - \sin^2 \theta_i}} \right|^2, \quad (2.9)$$

$$\epsilon_{PosV} = 1 - \left| \frac{\kappa \cos \theta_i - \sqrt{\kappa - \sin^2 \theta_i}}{\kappa \cos \theta_i + \sqrt{\kappa - \sin^2 \theta_i}} \right|^2, \quad (2.10)$$

where ε_{Pos_v} is the range of possible emissivity constants for the vertical polarization, ε_{Pos_h} is the range of possible emissivity constants for the horizontal polarization, and κ is the dielectric constant, the emissivity is calculated. The soil moisture is then found by selecting the soil moisture that corresponds to the possible dielectric constants that is closest to the dielectric constants calculated using the brightness temperature.

2.2.2 rSIR

Measurement Response Function

The brightness temperature measurement response function (MRF) is derived directly from the antenna beam pattern. Because of this, the response function is very similar for every measurement but rotates or tilts at different angles over the swath. The function is approximated using a multi-dimensional, elliptical, Gaussian curve.

$$G_s(\theta, \phi) = T_p^{-1} \int_0^{T_p} G(\theta, \phi + \omega_r t) dt, \quad (2.11)$$

where G_s is the effective antenna gain pattern that accounts for the smeared effect. This smeared effect is caused by the rotating radiometer beam [20]. G is the instantaneous gain pattern. This integral reflects the smeared antenna pattern that is caused by the rotations of the receiving dish. This is because the dish must integrate the received signal over a period of time T_p . Using this smeared antenna gain pattern the measurement response function can be calculated

$$\text{MRF}(x, y) = G_b^{-1} G_s(x, y), \quad (2.12)$$

where G_s is the smeared antenna gain pattern mapped onto the Cartesian coordinate grid, and G_b is the spatially integrated gain over the surface

$$G_b = \iint G_s(x, y) dx dy. \quad (2.13)$$

The MRF is used to improve the spatial resolution of the reconstructed image. This is accomplished through using the relationship of the brightness temperature at each pixel of the MRF and the

brightness temperature measurement. The MRF enables image reconstruction with pixels smaller than the measurement footprint. The relationship between measurement and footprint is

$$z = \iint \text{MRF}(x,y) T_B(x,y) dx dy, \quad (2.14)$$

where z an individual brightness temperature measurement. An example of a brightness temperature MRF for the SMAP radiometer used is shown in Fig. 2.5 and Fig. 2.6.

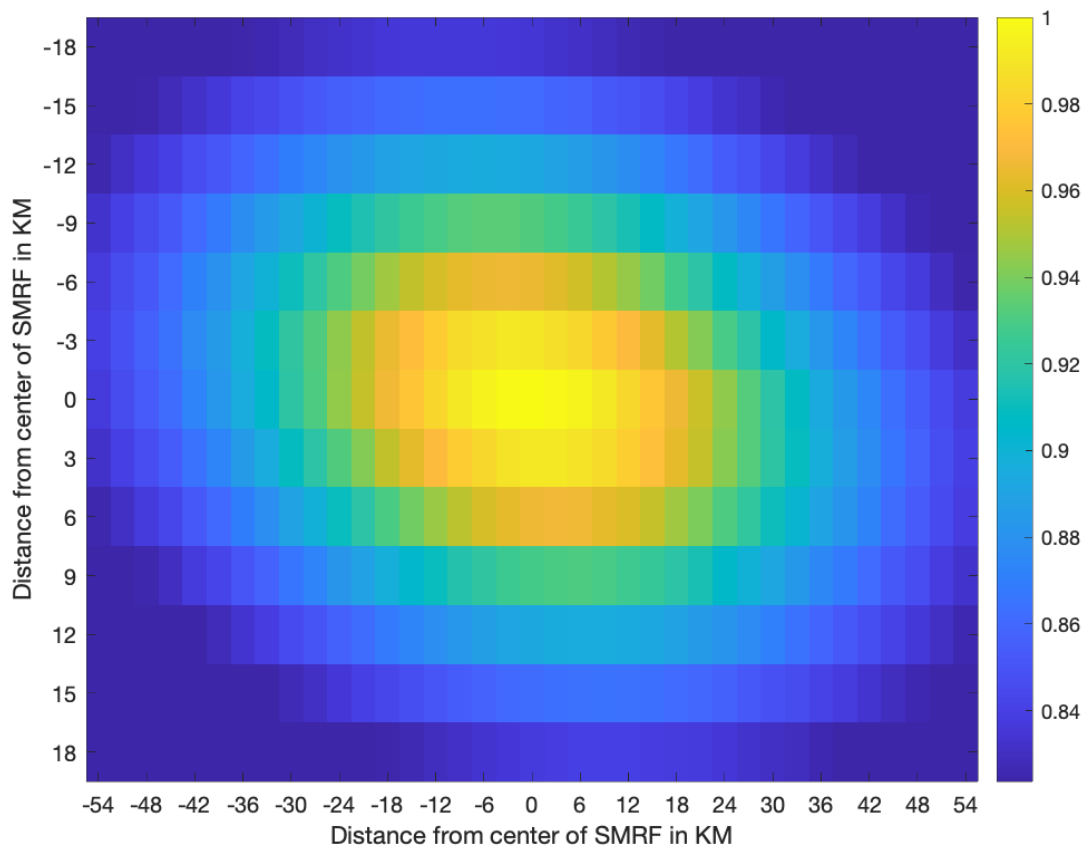


Figure 2.5: An example image of the MRF used. This is taken from day 276 of 2016.

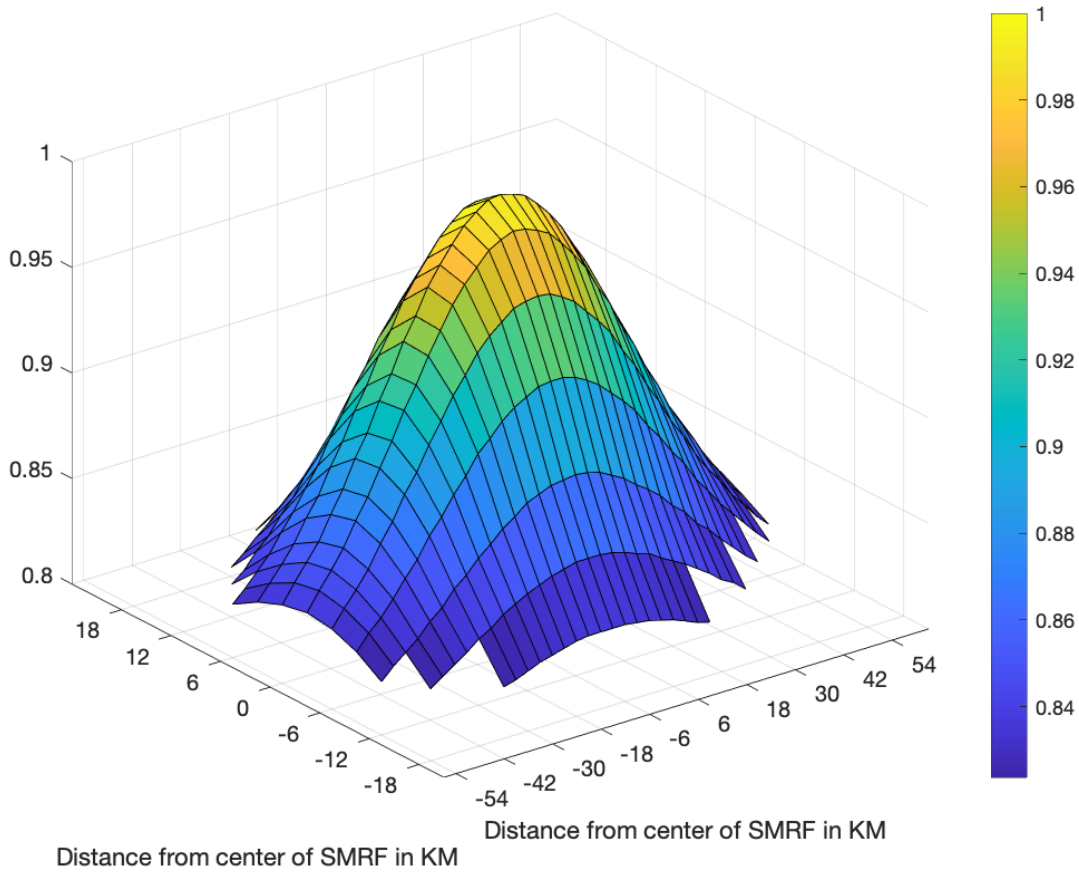


Figure 2.6: A surface plot of an example SMAP MRF used.

rSIR Iterative Update

The SIR algorithm is a maximum entropy iterative reconstruction technique that utilizes the antenna pattern to reconstruct high resolution images [11]. This measurement response function can be thought of as the contributions from a large number of point sources for each measurement.

The SIR reconstruction begins with the measurement equation

$$z_{x,y} = \sum_{x,y \in \text{image}} h_{x,y} a_{x,y}, \quad (2.15)$$

where $z_{x,y}$ is the noisy measurement, $h_{x,y}$ is the response function at a given pixel, and $a_{x,y}$ is the pixel value. In order to simplify the problem, the square image is unrolled into a single vector,

indexed by j , where $j = l + N_x k$. This problem can now be written in a matrix form

$$\vec{T} = \mathbf{H}\vec{a}. \quad (2.16)$$

In effect the rSIR algorithm inverts Eq. 2.16 using an iterative approach. For the first iteration, the average image is computed

$$a_j^0 = \frac{\sum_i h_{i,j} z_i}{\sum_i h_{i,j}}, \quad (2.17)$$

where a_j^0 represents the pixel value at j for the zeroth iteration. For all following k iterations, the value for a_j^k is calculated using a separate set of equations. The next iteration, a_j^{k+1} is calculated [11]

$$f_i^k = \frac{\sum_n h_{i,n} a_n^k}{\sum_n h_{i,n}} \quad (2.18)$$

$$d_i^k = \sqrt{\frac{z_i}{f_i^k}} \quad (2.19)$$

$$u_{i,j}^k = \begin{cases} \left[\frac{1}{2f_i^k} \left(1 - \frac{1}{d_i^k} \right) + \frac{1}{a_j^k d_i^k} \right]^{-1}, & d_i^k \geq 1 \\ \left[\frac{1}{2} f_i^k (1 - d_i^k) + a_j^k d_i^k \right], & d_i^k < 1 \end{cases} \quad (2.20)$$

$$a_j^{k+1} = \frac{\sum_i h_{i,j} u_{i,j}^k}{\sum_i h_{i,j}}. \quad (2.21)$$

This calculation begins with the forward projection f_i^k . Then d_i^k is the square root of the ratio of the current image with its forward projection. Depending on this ratio, and update is calculated in Eq. 2.20. This non-linearity is performed to prevent excessively large updates from being calculated. The image is then updated in using Eq. 2.21.

The rSIR algorithm iteratively improves the image resolution at the cost of amplifying noise in the image. In execution, the rSIR algorithm is terminated before it converges to a final solution to balance the amount of noise amplification that occurs. The rSIR algorithm is capable of producing fine resolution brightness temperature images. While the SMAP data products are limited to a resolution of 9 km x 9 km pixels and 36 km x 36 km pixels, the rSIR enables the creation of 3 km x 3 km pixel images [11].

The rSIR algorithm is applied to SMAP data. The rSIR algorithm enables multiple reconstruction resolutions. Possible output resolutions include 36 km x 36 km, 9 km x 9 km, and 3 km x 3 km pixel sizes. Examples of these three resolutions are shown in Fig. 2.7, 2.8, and 2.9. The focus of this thesis is 3 km brightness temperature and soil moisture images.

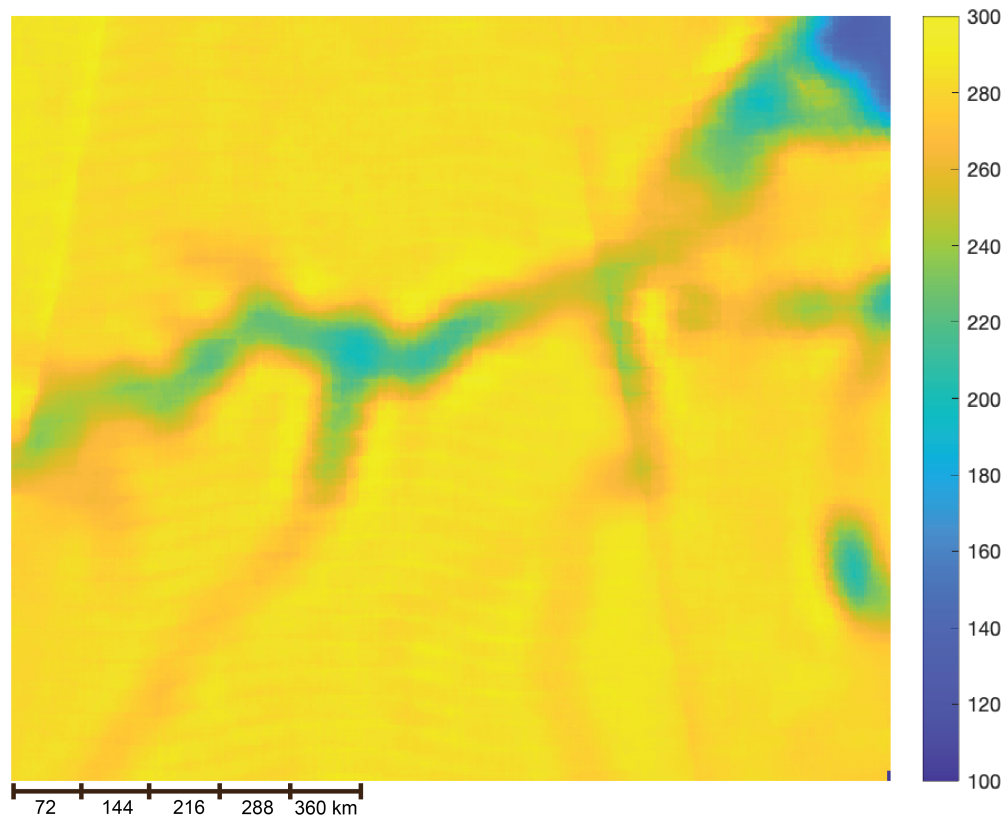


Figure 2.7: rSIR image made using SMAP data from day 276 of 2016. This is made using a 3-km pixel size. The effective resolution is coarser than the pixel size. This image is zoomed in over the mouth of the Amazon river to show various details in the image.

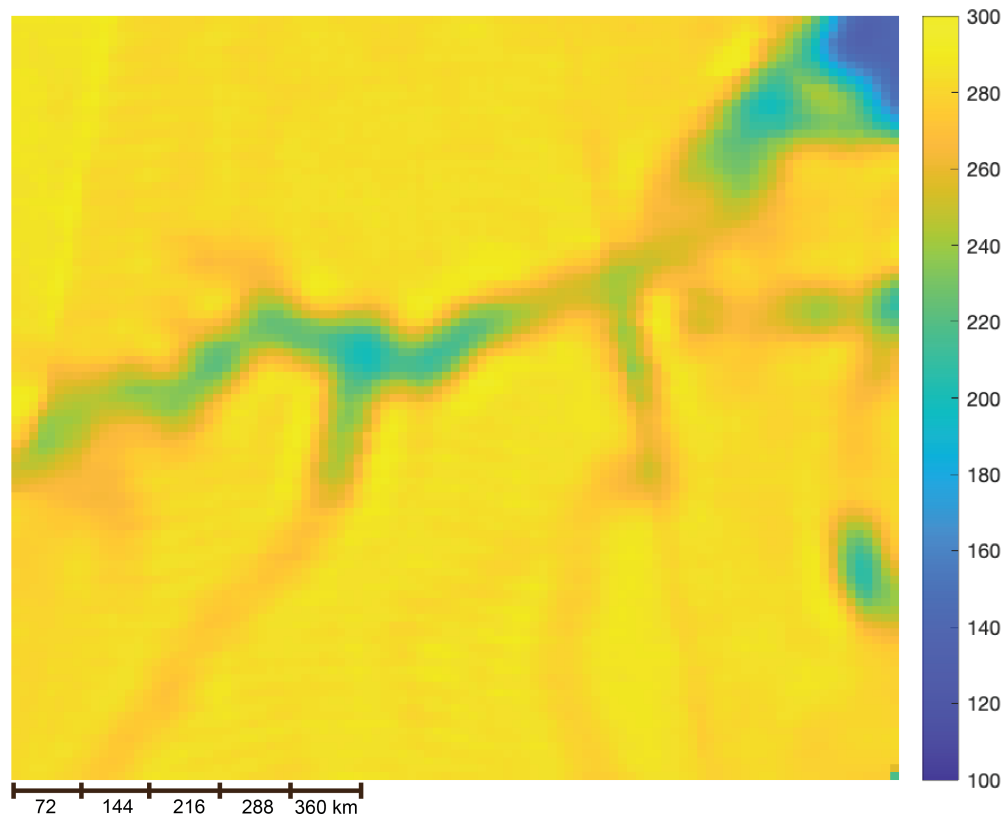


Figure 2.8: rSIR image made using SMAP data from day 276 of 2016. This is made using a 9-km pixels size. This image is zoomed in over the mouth of the Amazon river to show various details in the image. There is an increase in pixelization on the borders of the river.

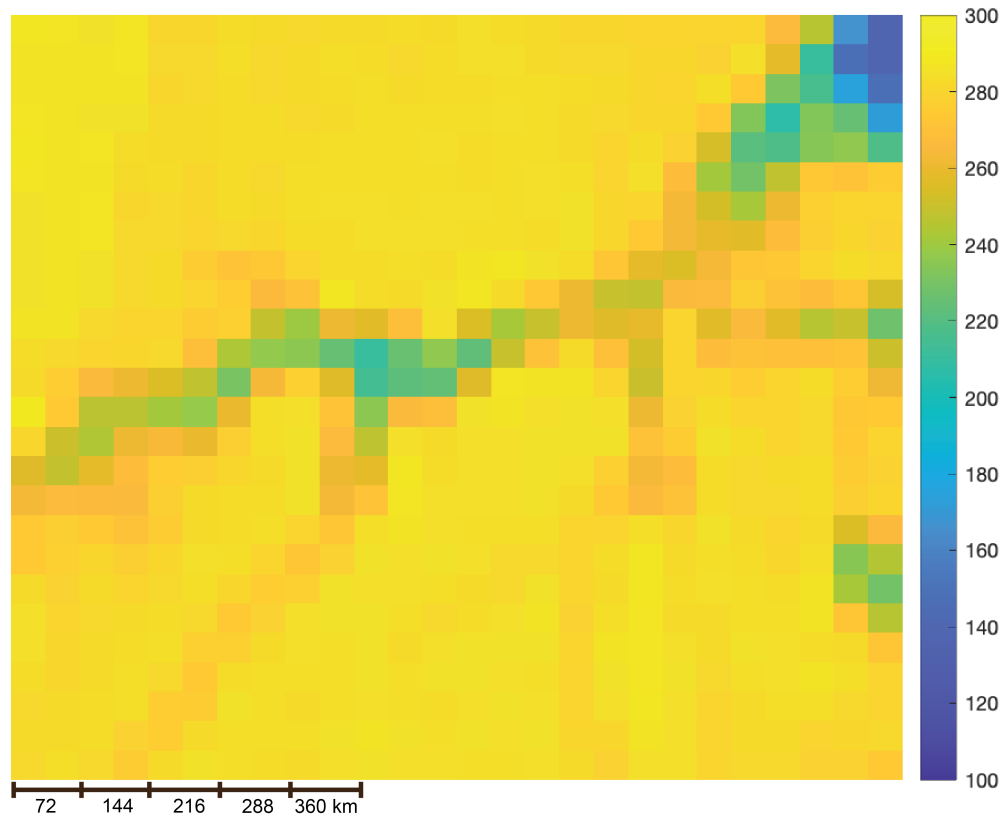


Figure 2.9: Drop-in-the-bucket gridded image made using SMAP data from day 276 of 2016. This is made using a 36-km pixels size. This image is zoomed in over the mouth of the Amazon river to show various details in the image. In this case, there is extreme pixelization. This pixel size corresponds with the radiometer footprint size.

2.3 rSIR Integration

The rSIR algorithm is used extensively through this thesis. In later chapters, variations of the rSIR algorithm are discussed and evaluated. The ultimate goal of this thesis is to derive a version of the rSIR algorithm that enables high resolution soil moisture image reconstruction.

CHAPTER 3. ALGORITHM OVERVIEW AND SIMULATIONS

I consider two families of approaches to combining the rSIR algorithm with the soil moisture algorithm. Traditionally, the rSIR algorithm calculates estimate updates in the measurement space, i.e., in brightness temperature [21]. However, it is possible to adapt the rSIR algorithm to calculate updates in the derived parameter space, i.e., in soil moisture. Fundamentally, the update in the rSIR algorithm can be calculated in either brightness temperature or soil moisture. I hypothesize that there is a performance improvement using a combined rSIR and soil moisture algorithm when compared to traditional sequential methods. This chapter provides an overview of the newly adapted algorithms tested, and examines simulations done to determine how various combinations of the rSIR and non-linearly derived parameters behave.

3.1 Non-Linear Characteristics of the rSIR and Soil Moisture Algorithm

The rSIR and soil moisture algorithms are non-linear functions. The rSIR algorithm has a non-linearity introduced by Eq. 2.20. The soil moisture algorithm has a non-linearity introduced in Eq. 2.6, 2.9, and 2.10. When combined, the two algorithms have the attribute

$$f(g(x)) \neq g(f(x)), \quad (3.1)$$

where $f(x)$ represents the rSIR algorithm and $g(x)$ represents the soil moisture algorithm. This forms the theoretical basis for this exploration. Because the two algorithms are both non-linear functions, I expect different results when combining the two algorithms. This thesis, in essence, attempts to derive a new function $h(x)$ that replaces the sequential computation of soil moisture, $g(f(x))$. To test this, I first derive the new algorithms and test them using simplified simulations. Later chapters consider these algorithms with actual SMAP data.

3.2 Sequential rSIR Soil Moisture Algorithm

The sequential rSIR soil moisture algorithm is a common approach that first reconstructs the brightness temperature measurements using rSIR and then uses these reconstructed images in the soil moisture algorithm. Fig. 3.1 illustrates this algorithm. The sequential rSIR algorithm reconstructs a brightness temperature image of 3 kilometer pixel size [22].

Sequential rSIR Soil Moisture Algorithm

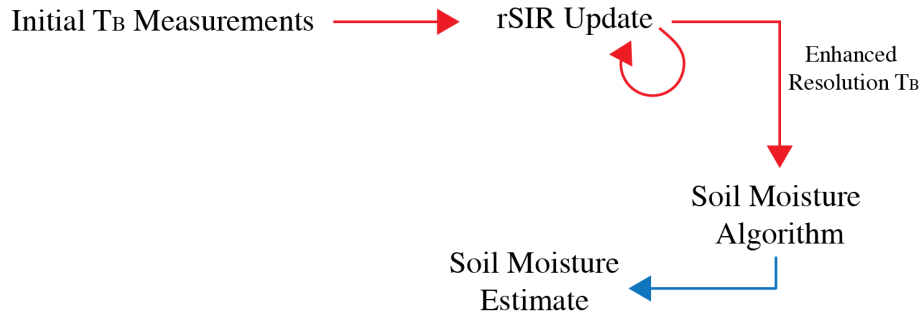


Figure 3.1: Flowchart of the sequential rSIR soil moisture algorithm.

3.3 Soil Moisture form of rSIR

I term the first group of combined algorithms as the Soil Moisture form of rSIR (SMrSIR). This combination performs the iterative update calculations in brightness temperature space and requires only very minor changes to the rSIR algorithm. Fig. 3.2 illustrates this approach. This algorithm is expected to perform similarly to the sequential rSIR soil moisture algorithm as the update is still calculated in brightness temperature space. Once the update is calculated, it is converted to soil moisture and then added into the pixel value for that iteration. In other words, Eq. 2.20 is calculated in brightness temperature, and the resulting $u_{i,j}^k$ is converted to soil moisture. Then Eq. 2.21 is computed in soil moisture space.

SMrSIR Algorithm

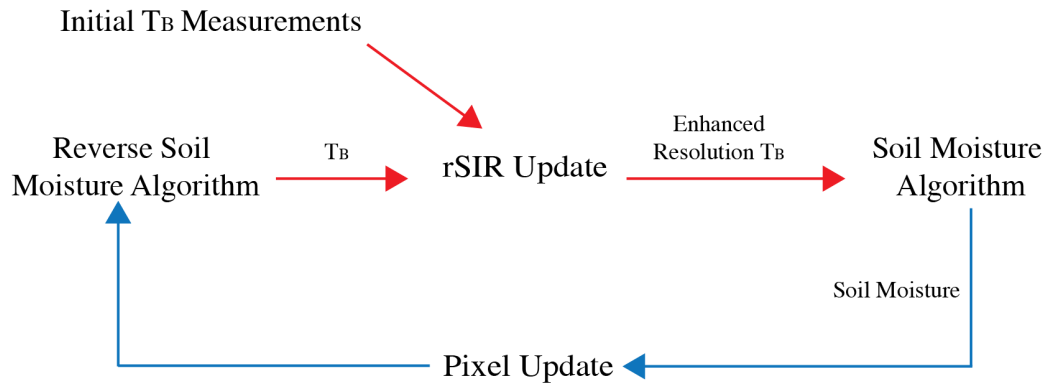


Figure 3.2: Flowchart of the SMrSIR algorithm approach.

3.4 Soil Moisture Image Reconstruction

I term the second group of combined algorithms as the Soil Moisture Image Reconstruction (SMIR) algorithms. This combination calculates the update in soil moisture space and requires a more complex adaption of the rSIR algorithm. This algorithm is illustrated in Fig. 3.3. This algorithm first produces an average brightness temperature image that is on the 3 kilometer grid, that has not yet resolved the high resolution details in the estimate. I then experiment with changes to the measurement response function (MRF). I ultimately create a soil moisture response function that enables greater amount of detail to be resolved. This is discussed further in Chapter 5.

The sequential rSIR soil moisture, the SMrSIR, and the SMIR algorithms all have the capability to produce soil moisture estimates over the entire SMAP swath. This is a significant benefit when compared to the JPL disaggregation algorithm that is restricted to the overlap between the SENTINEL-1 and SMAP swaths and results in minimal spatial coverage. The following sections illustrate the differences between these three methods.

3.5 Simulations

In this section, I run simulations in order to confirm how well rSIR performs when combined with general non-linear transformations. These non-linear transformations represent sim-

SMIR Algorithm

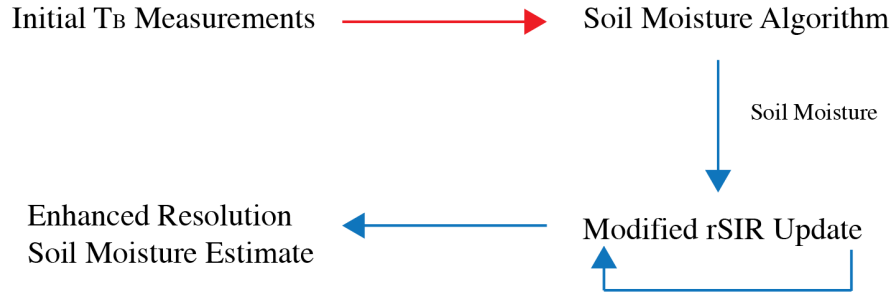


Figure 3.3: Flowchart of the SMIR algorithm.

plified versions of the soil moisture algorithm. This simulation is a toy problem performed to highlight the potential differences among the three algorithms and to ensure rSIR performs well in a parameter space. This simulation illustrates the effects a non-linear function would have when combined with the rSIR algorithm.

These simulations have the benefit of having a truth image that the results can be compared to. The brightness temperature and soil moisture truth images are shown in Fig. 3.4 and 3.5. These truth images are used to compute errors and determine how well the algorithms are able to reproduce the truth image. The brightness temperature truth image is converted from brightness temperature to soil moisture. In this initial simulation a simplified soil moisture algorithm is used, which is defined as

$$M_S = \exp\left(\frac{T_B}{300}\right) + 5, \quad (3.2)$$

where M_S is the soil moisture and T_B is the brightness temperature. While this is an overly simplified expression, it represents a non-linear transformation between brightness temperature and soil moisture.

The sequential rSIR soil moisture algorithm is also performed on the simulation data as a means of comparison. This is done using the rSIR algorithm on brightness temperature measurements for fifty iterations. Fifty iterations were chosen as a stopping point for easy comparison.

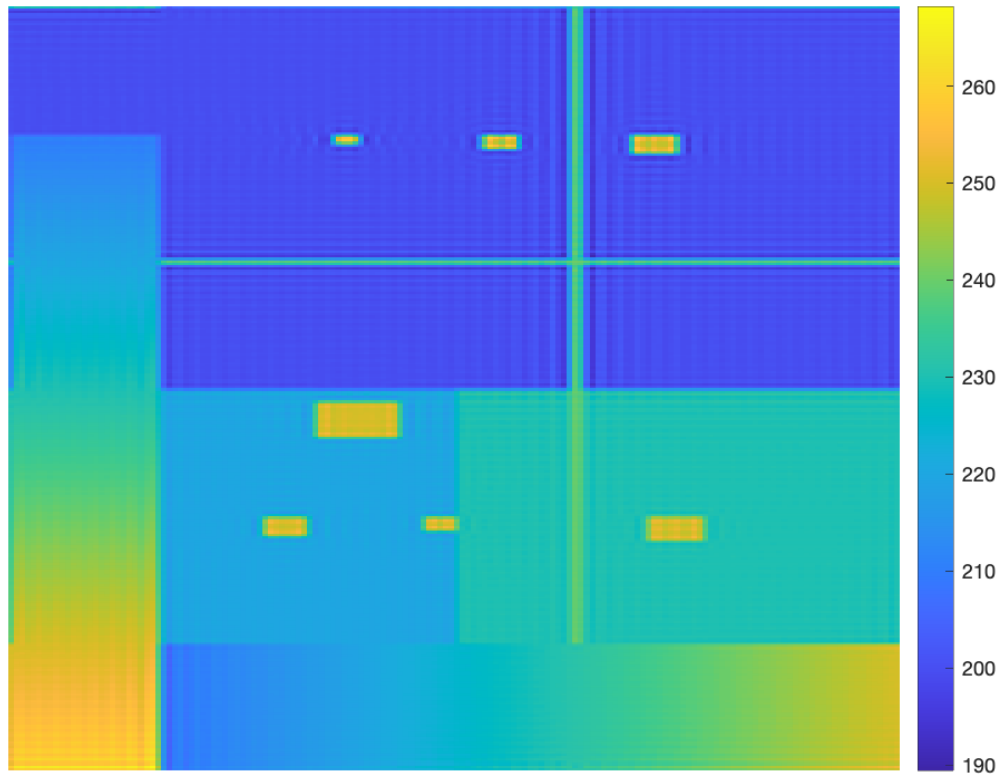


Figure 3.4: Brightness temperature truth image for simulations. Radiometer measurements are simulated by sampling this image according to the SMAP geometry.

When real data is used, the number of optimal iterations is found experimentally. The rSIR algorithm will eventually converge to a solution at the cost of amplifying the noise in the image. A balance is found for each individual sensor. The resulting brightness temperature image is then transformed using the simplified soil moisture algorithm. The results are shown in Fig. 3.7.

The simulation is run on a simulated 3 km pixel grid. A MRF (Fig. 3.6) that matches the theoretical SMAP MRF is used. The footprint is 30 kilometers in diameter. The MRF has a 30 kilometer footprint in the center and pixels that are 3 km wide, resulting in a 90 km x 90 km measurement function.

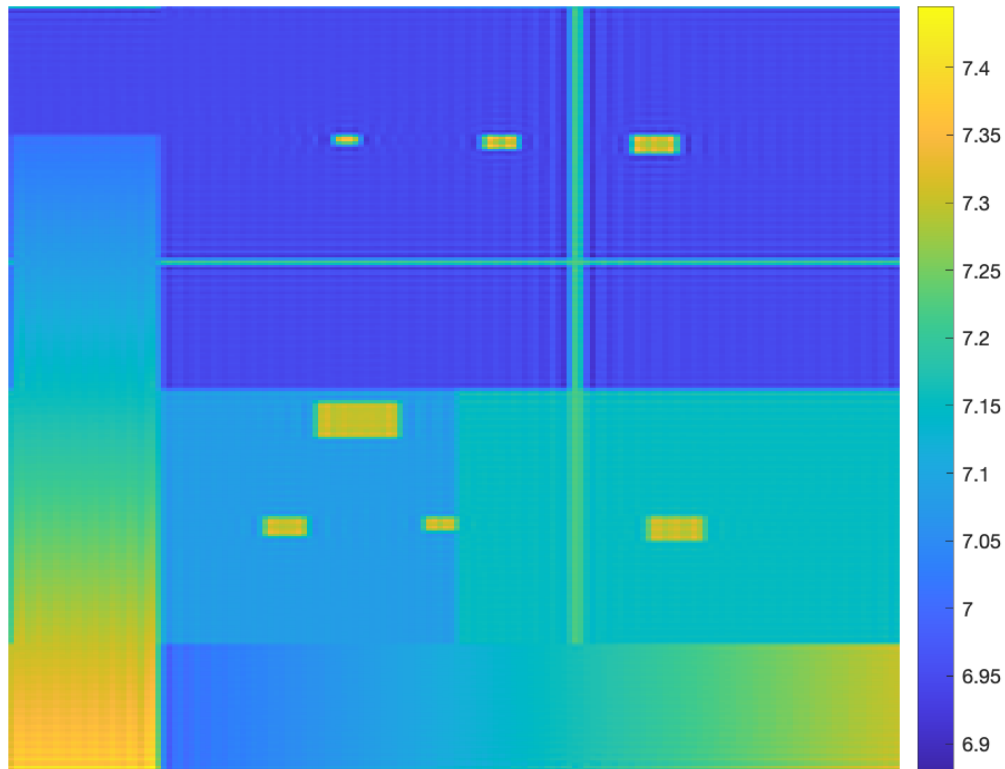


Figure 3.5: Soil moisture truth image produced using the simplified soil moisture transformation. Radiometer measurements in Eq. 2.16 are simulated by sampling the brightness temperature in Fig. 3.4.

3.5.1 SMrSIR Simulation

The SMrSIR algorithm is first tested. As previously noted this method has the benefit that few changes are required to combine the current sequential algorithm. The simulation is run by sampling the truth image shown in Fig. 3.4. This is done using simulated geometries that closely resemble SMAP, i.e., the simulation uses nearly identical MRF's and samples using a rotating beam radiometer.

This method is expected to produce images that are similar to the sequential algorithm. This is because the forward and reverse soil moisture transformations are very precise in the simulation. The difference between this method and the sequential algorithm is computed in Fig. 3.9, while the results of the SMrSIR algorithm can be seen in Fig. 3.8. While slight, there is a small dif-

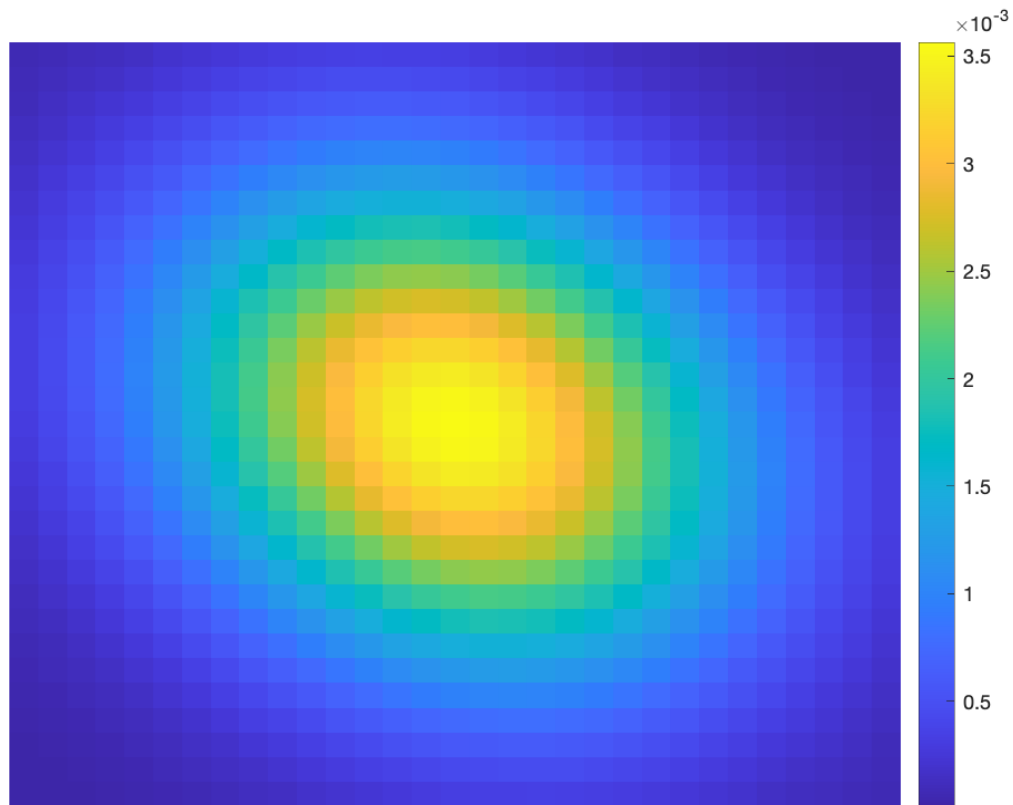


Figure 3.6: Example of a simulation MRF. This MRF is similar to a typical MRF used by the SMAP sensor.

ference between the two methods. Upon further analysis, this difference reduced the overall error between the reconstructed soil moisture estimate and the true soil moisture estimate. This is encouraging because it shows that there could be an improvement made using a combined approach to calculating soil moisture.

3.5.2 SMIR Simulation

The SMIR algorithm is also simulated. This method is created by transforming the individual brightness temperature measurements to soil moisture before applying the rSIR algorithm. This simulation enables testing of this method without reformulating the measurement response function (MRF) for soil moisture. However, when real data is used, it is likely that a MRF that is

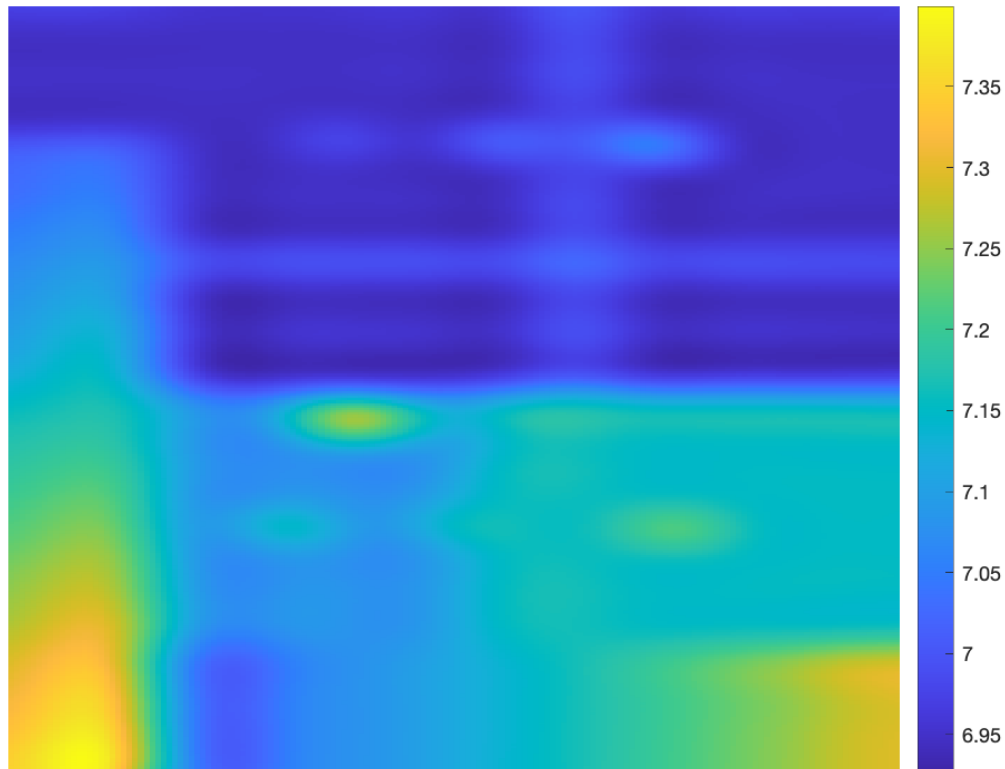


Figure 3.7: Simulation results for the sequential rSIR soil moisture algorithm.

tailored to soil moisture is required. The results of this simulation are shown in Fig. 3.10 and 3.11. In general, the SMIR outperforms the sequential rSIR soil moisture algorithm but had slightly larger error when compared with the SMrSIR algorithm.

3.5.3 Simulation Results

The results of both simulations are analyzed in Table 3.1. Using the mean and root mean square error I am able to determine that there is a slight improvement when using either of the combined rSIR algorithms when compared with the sequential rSIR soil moisture algorithm. This encourages further analysis using real data. This is done in the next section.

Ultimately the three algorithms perform similarly in this toy problem with no noise. The SMrSIR and SMIR algorithms have a slight performance increase when compared with the se-

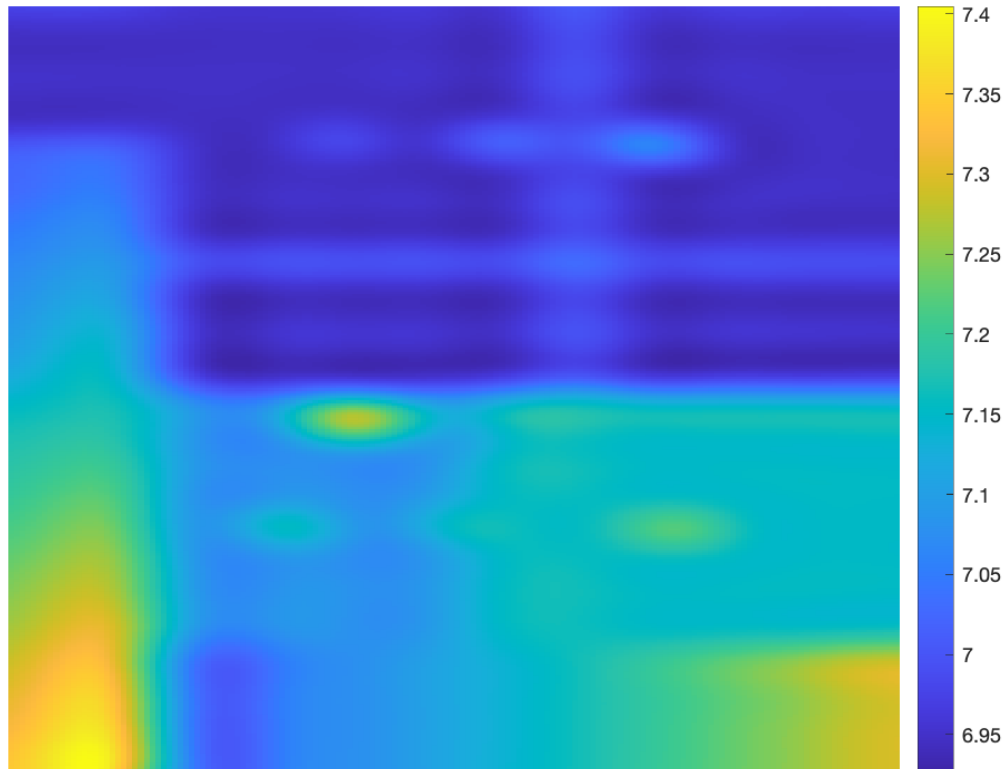


Figure 3.8: Soil moisture result of the combined rSIR algorithm using a brightness temperature update after 50 iterations using the simplified soil moisture algorithm described in Eq. 3.2.

Table 3.1: Summary of simulation errors for the various different methods after 50 rSIR iterations. While small, there is a slight improvement in the errors of the combined rSIR soil moisture algorithms compared with the sequential rSIR soil moisture algorithm. This improvement warrants a deeper investigation.

Method	Mean Error	RMS Error
Sequential	0.0180	0.0366
Combined with TB Update	0.0179	0.0359
Combined with Soil Moisture Update	0.0179	0.0363

quential rSIR soil moisture algorithm. However, this simulation is a toy problem to experiment with rSIR and parameters computed using non-linear transformations. In the following chapters the SMrSIR and SMIR are tested using real data.

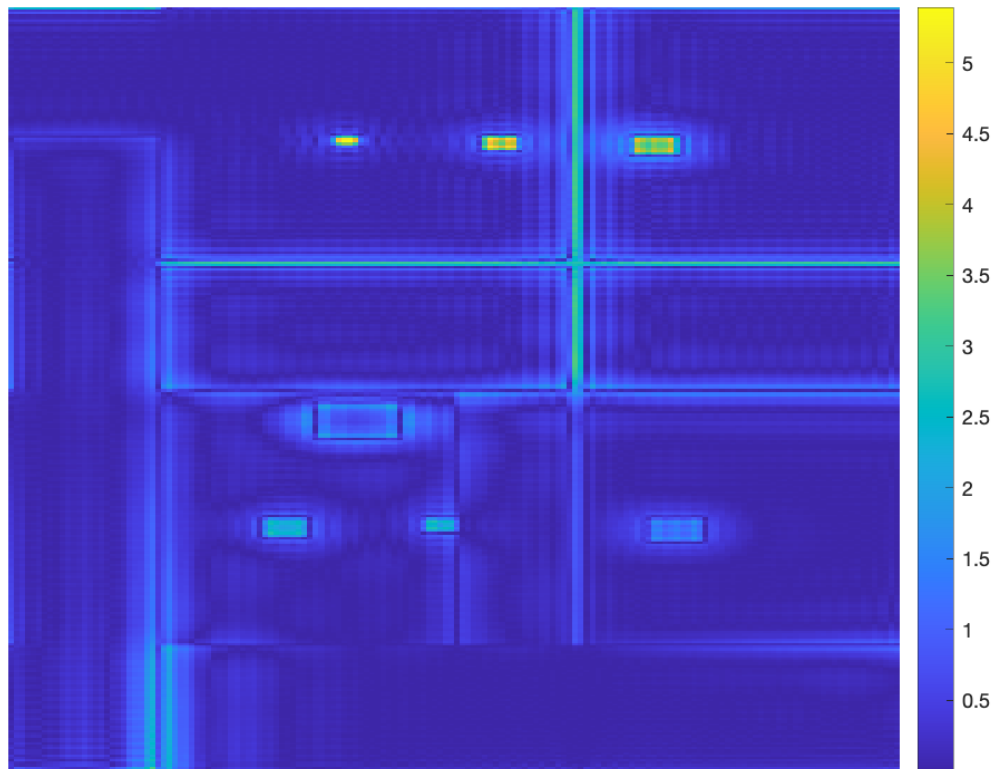


Figure 3.9: Percent error between the SMrSIR output and the truth image for the simulation.

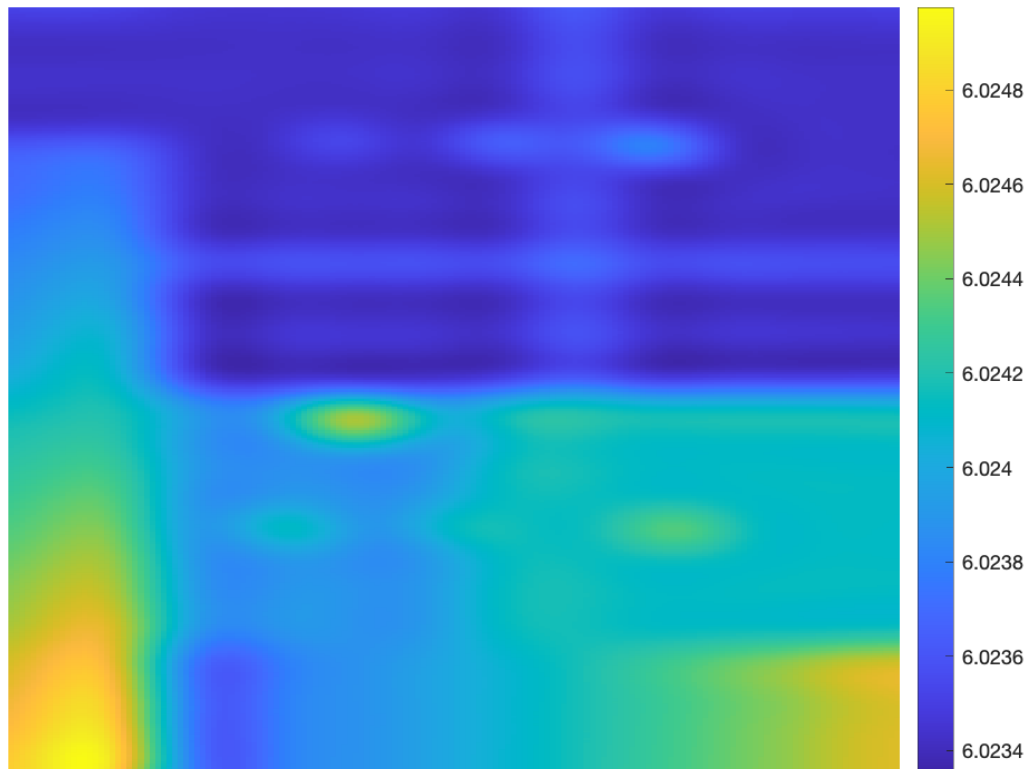


Figure 3.10: Result of a combined rSIR algorithm using a soil moisture update after 50 iterations.

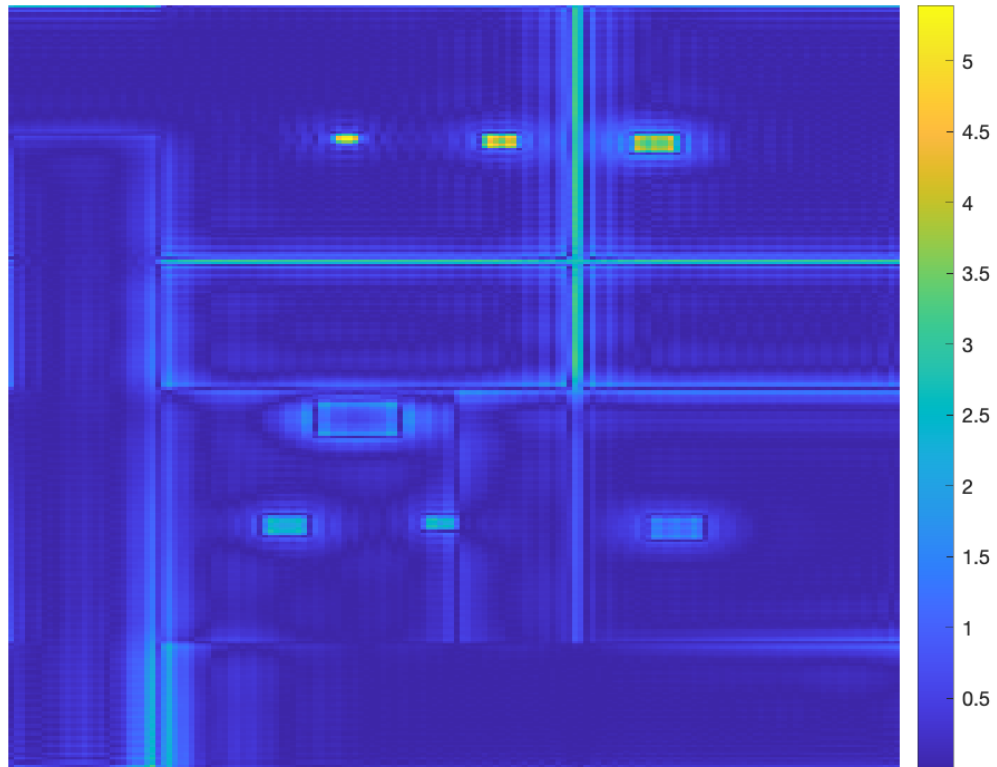


Figure 3.11: Percent error between the SMIR output and the truth image for the simulation.

CHAPTER 4. RSIR UPDATES USING BRIGHTNESS TEMPERATURE MEASUREMENTS

4.1 SMrSIR

In this chapter I explore the Soil Moisture form of the rSIR (SMrSIR) that was discussed in the previous chapter when applied to actual SMAP data. This method is explored first due to the simpler implementation when compared with the Soil Moisture Image Reconstruction (SMIR) algorithm. This method initially computes a soil moisture image from the average T_B image. It then calculates an update in brightness temperature, which is then transformed into soil moisture and fed into the pixel update. The average brightness temperature image is on the 3 km grid but has a relatively low resolution. This results in a low resolution soil moisture estimate that is somewhat improved by the high resolution ancillary data. The SMrSIR is performed iteratively, where an update to the image is calculated during each iteration, improving the resolution and resolving finer details.

Calculating the update in a brightness temperature space does not require alteration to the rSIR algorithm. However, this approach requires the derivation and usage of an inverse of the soil moisture algorithm. This is required as the soil moisture image must be converted to brightness temperature during each iteration so that an update in brightness temperature can be calculated. As the soil moisture algorithm inverse is non-trivial, the derivation of the inverse soil moisture algorithm is provided.

4.1.1 Reverse Soil Moisture Transformation

The reverse soil moisture transformation is used to transform soil moisture estimates into brightness temperature estimates. This is needed when rSIR is used to estimate soil moisture while calculating the iterative updates in brightness temperature.

The reverse soil moisture transformation begins with the dielectric mixing model. Because we start with a soil moisture estimate, we do not need to compute a range of dielectric constants. We just have a singular dielectric that corresponds with the soil moisture estimate. Using this dielectric, the emissivity is calculated

$$\varepsilon = 1 - \left| \frac{\kappa \cos \theta_i - \sqrt{\kappa - \sin^2 \theta_i}}{\kappa \cos \theta_i + \sqrt{\kappa - \sin^2 \theta_i}} \right|^2, \quad (4.1)$$

where ε is the emissivity constants, κ is the dielectric constant, and θ_i is the incidence angle [6]. The surface roughness effects are then added into the emissivity constant

$$\varepsilon = \frac{\varepsilon - 1}{e^h \cos^2 \theta_i} + 1, \quad (4.2)$$

where h is the surface roughness, supplied from ancillary data sets. The vegetation effects are then added to the constant

$$\varepsilon = \varepsilon (T_C^2 + \alpha T_C - \alpha T_C^2) + 1 - T_C^2 - \alpha + \alpha T_C^2, \quad (4.3)$$

where α is the albedo, and T_C is the canopy transitivity, supplied from ancillary data sets. Brightness temperature is then calculated using the corrected ε

$$T_B = \varepsilon T_P, \quad (4.4)$$

where T_B is the brightness temperature, and T_P is the physical surface temperature, supplied by ancillary data sets.

When ancillary data is missing, it is flagged and removed from the processing. This is done to prevent missing data from skewing the results.

4.2 SMrSIR Results

4.2.1 Area of Study

In this thesis a small subsection of the full global image is studied. This area is depicted in Fig. 4.1. This area is an approximately 900 kilometer by 900 kilometer area. This area was chosen for its wide range of features and values, including rivers, lakes, and dry plains.

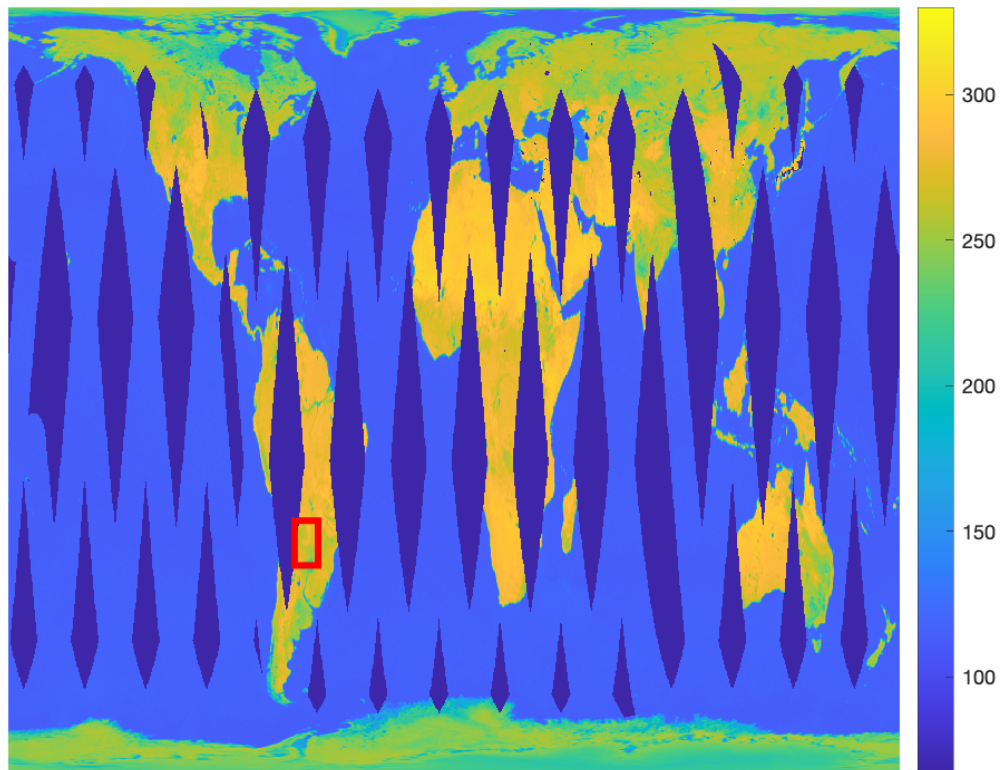


Figure 4.1: Global image with a bounding box around the area of study. This area is chosen because it has a wide range of soil moisture values and many features that are resolved. This image is made using data from day 276 of 2016.

4.2.2 Results

The SMrSIR begins by running the rSIR algorithm unchanged for a predetermined number of iterations. Allowing the rSIR algorithm to run a few iterations in order to begin converging to its brightness temperature solution before the soil moisture transformation begins improves the results. This is due to the fact that the soil moisture algorithm is very sensitive to small changes in brightness temperature. In some cases, the initial estimate produced by the rSIR is clipped by the limited dynamic range of the soil moisture algorithm. Five iterations are found to be sufficient.

After the initial five rSIR iterations, the soil moisture algorithm is included. It begins by converting the output of the last calculated rSIR iteration into soil moisture and begins the SMrSIR algorithm.

This method takes full advantage of the high resolution ancillary data. However, there is some quantization error that occurs in the soil moisture algorithm. This is introduced in the forward transformation during the step that minimizes the error between the theoretical and calculated emissivity. This ultimately prevents iterative rSIR from moving towards a final solution as the updates are too small. In order to ensure convergence, a more granular soil moisture estimation is used during the forward transformation. Despite this change, the estimation fails to update and does not continue to converge to a final solution. The final results of the SMrSIR algorithm can be seen in Fig. 4.2.

4.3 Analysis

We find that the combined rSIR-soil-moisture algorithm that updates in brightness temperature performs poorly. This is because this method introduces a great deal of computation error with little improvement to the soil moisture estimate. Because the estimate is converted to soil moisture, and then immediately converted back to brightness temperature, the estimate has quantization error due to the limited granularity of the forward soil moisture transformation. This approach is therefore fundamentally flawed.

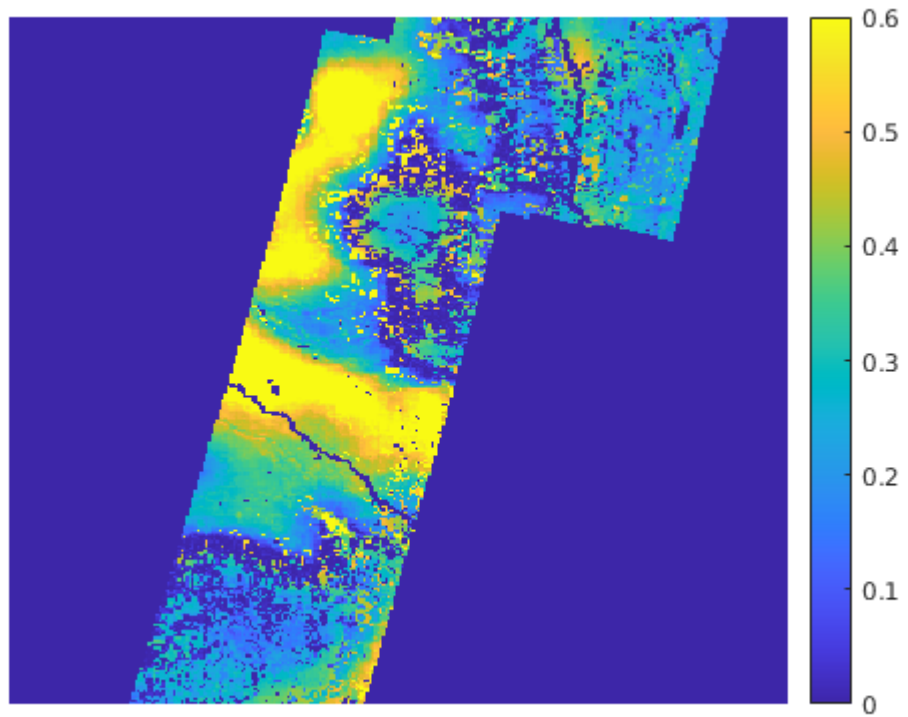


Figure 4.2: Figure showing the results of the combined rSIR and soil moisture algorithm. This data is taken from day 276 of 2016. This figure shows some of the quantization error. Fig. 4.1 shows the area of study in this thesis. This sub-image is approximately 900 by 900 kilometers.

CHAPTER 5. RSIR UPDATES USING SOIL MOISTURE MEASUREMENTS

The combined rSIR algorithm when the update is calculated using soil moisture measurements has the potential to outperform all the methods examined thus far in this thesis. As noted previously, I term this method the soil moisture image reconstruction algorithm (SMIR). This method is a more direct combination of the soil moisture and image reconstruction algorithms. Fewer conversions between brightness temperature and soil moisture are occurring, which results in lower error introduced by these conversions. I show in chapter 6 that the SMIR algorithm has a performance improvement when compared to other algorithms.

The SMIR algorithm has two main approaches. The first uses the brightness temperature measurement function (MRF) in the SMIR algorithm, and the second derives a novel soil moisture response function (SMRF) that is used in the rSIR algorithm. In this chapter, I more fully explore the SMIR algorithm. Multiple approaches to calculating SMRF's are proposed and their performance evaluated.

5.1 Update in Soil Moisture Space

The SMIR algorithms use soil moisture measurements that are calculated from raw brightness temperature measurements. Traditionally, the rSIR algorithm uses a brightness temperature measurement response function (MRF) that is derived from the antenna beam pattern [21]. This same MRF can be used in the SMIR algorithm, but using a soil moisture response function (SMRF) outperforms the brightness temperature MRF. Both methods are analyzed in this chapter. The results of each SMIR method are benchmarked with SENTINEL-1 soil moisture data product produced by NASA JPL. An example of the SENTINEL-1 soil moisture data product is shown in Fig. 5.1.

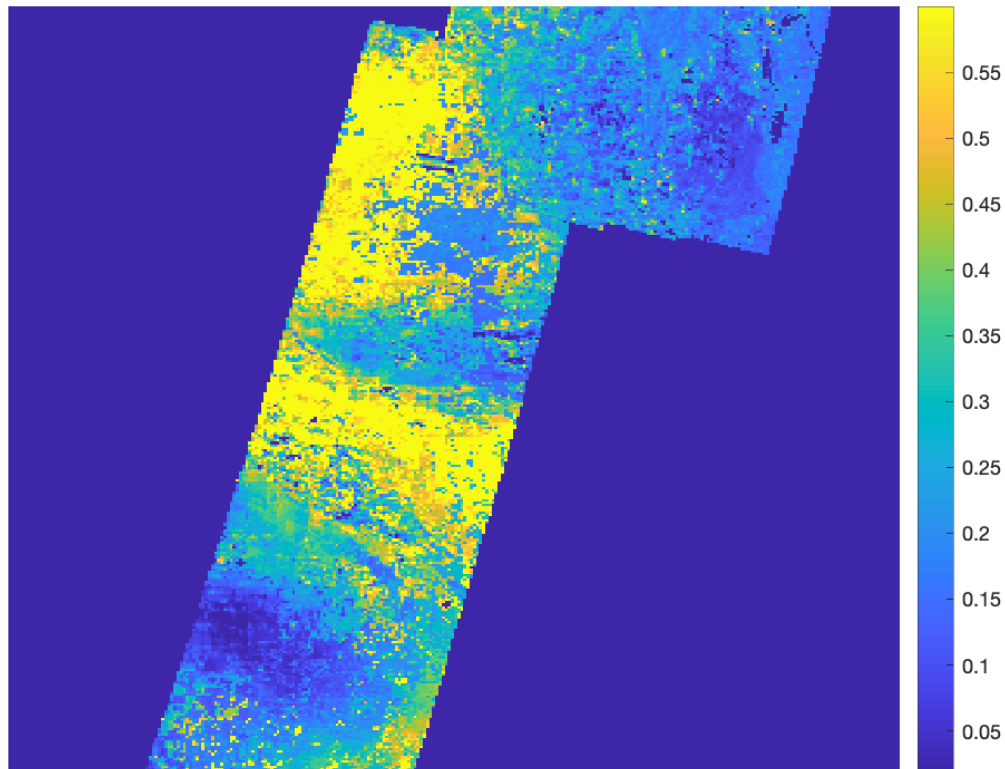


Figure 5.1: A SMAP-SENTINEL-1 soil moisture estimate produced by the SMAP team at the NSIDC. This sample corresponds with the data used in this chapter, sharing the same coverage and time. This data is from the 276 day of 2016. This image is made using 3 km pixels [2].

The results of the sequential algorithm are also provided for comparison in Fig. 5.2. These results are produced by first applying rSIR to brightness temperature measurements and then inputting the resulting image into the soil moisture algorithm.

5.1.1 Soil Moisture Measurements

Soil moisture measurements are made by converting the brightness temperature measurement into soil moisture estimates. A brightness temperature measurement is defined as the weighted

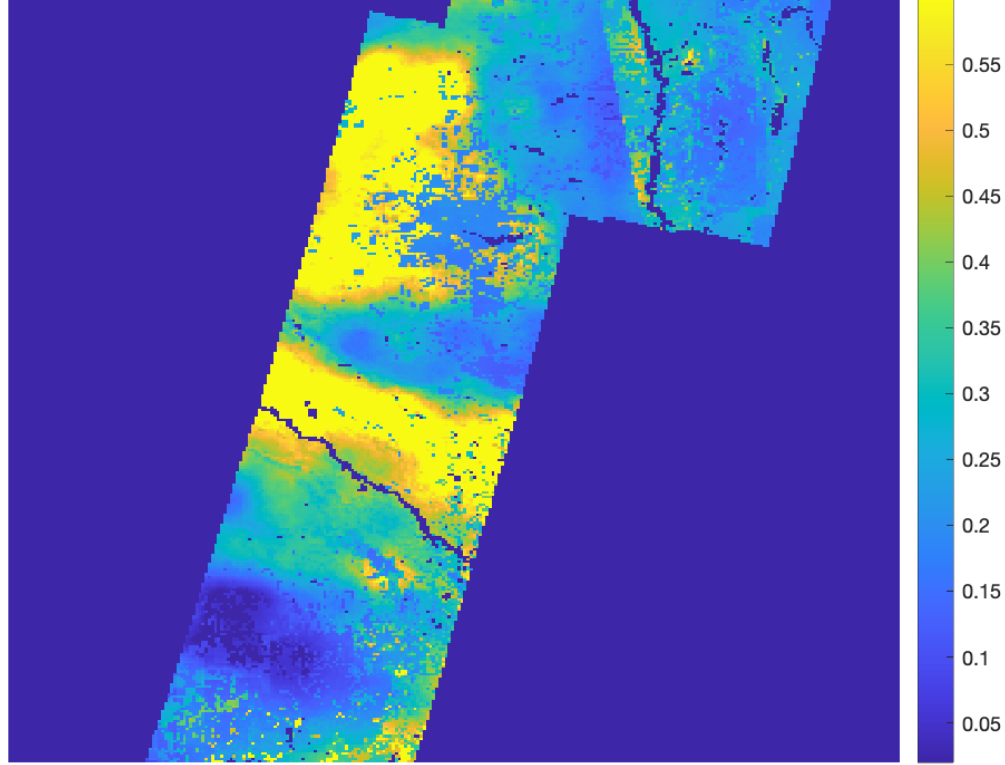


Figure 5.2: Results from the sequential algorithm. This image is made using data from day 276 of 2016.

sum over the entire brightness temperature measurement footprint

$$z = \sum_j h_j a_j, \quad (5.1)$$

where z is the measurement, h_j is the MRF, and a_j is a vector of the true brightness temperature values. Because these measurements are used in the rSIR algorithm, a soil moisture measurement analog is required in both versions of the SMIR algorithm.

Soil moisture measurements are made by inputting the brightness temperature measurements, and their collocated ancillary data measurements, into the soil moisture algorithm. This produces a vector of soil moisture measurements which is then fed into the SMIR algorithm.

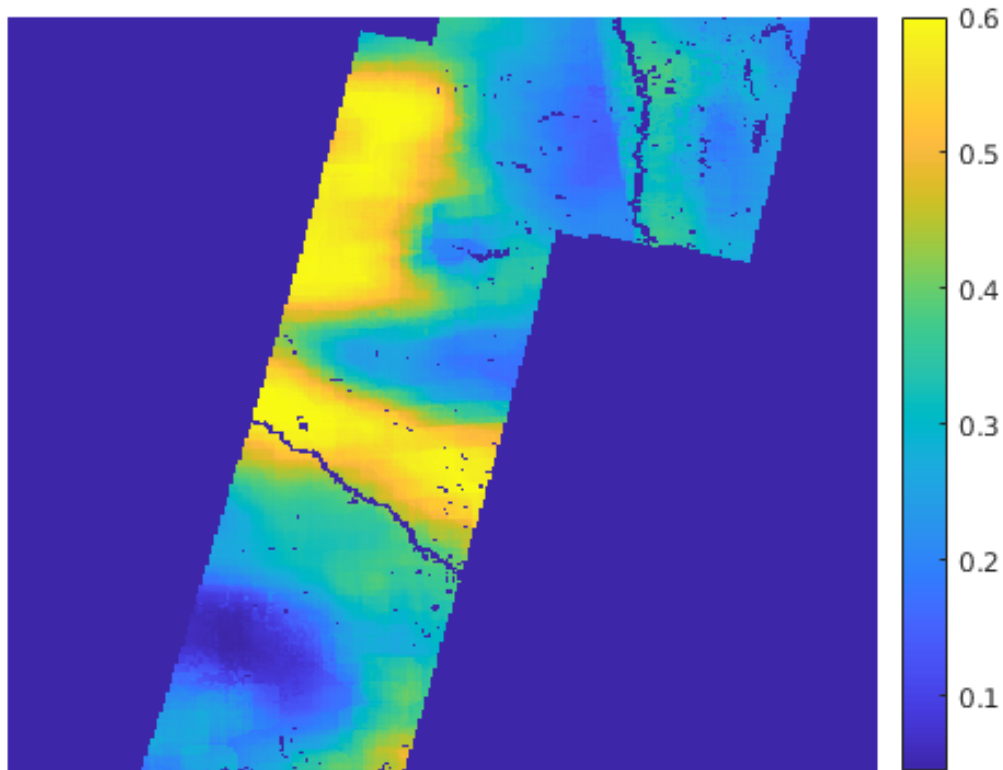


Figure 5.3: The AVE image produced using the soil moisture measurements and the brightness temperature MRF. This 3-km pixel image is made using data from day 276 of 2016.

5.1.2 Soil Moisture Update, using T_B Measurement Response Function

Both versions of the SMIR algorithm use soil moisture measurements and differ in the MRF used. The first version considered continues to use the brightness temperature MRF that is used in brightness temperature image reconstruction.

This direct method performs poorly. The initial average image (AVE) is shown in Fig. 5.3. In this image we can see poor detail resolution and a very smooth result. This is likely caused by how little of the high resolution ancillary data is used. The ancillary data is only used when the soil moisture measurements are computed. During this step, all the information contained in a measurement footprint is averaged together. This results in an overall smooth image. Further, limited high resolution detail is introduced by the rSIR algorithm as no new information is added. The results of iterating through the rSIR algorithm are shown in Fig. 5.4.

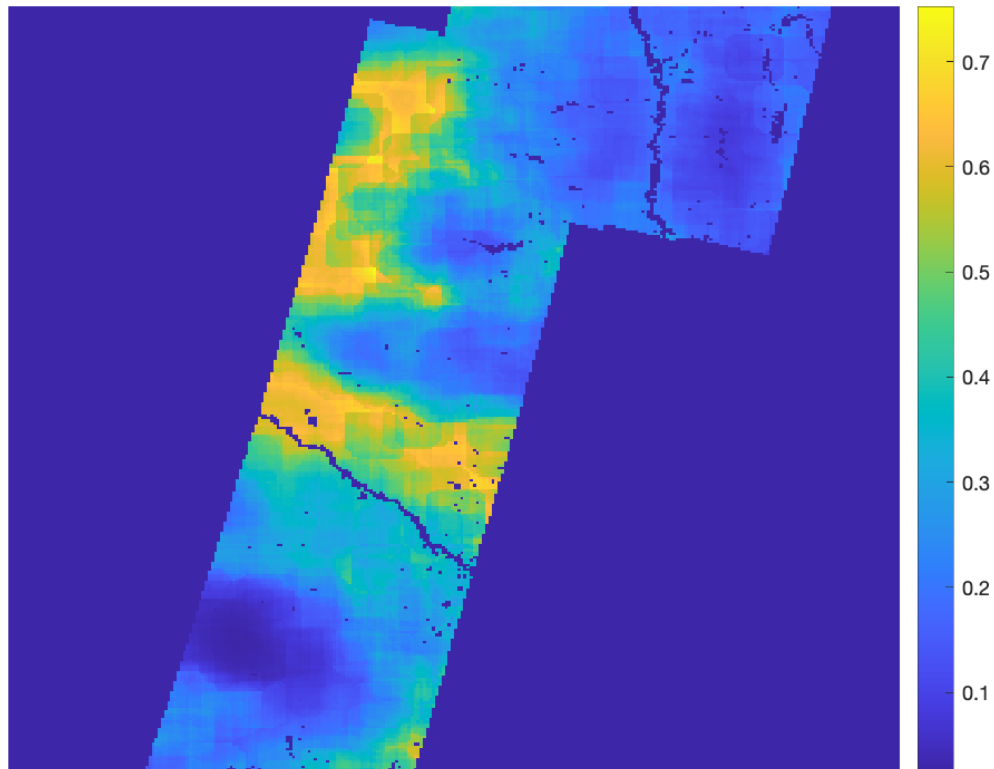


Figure 5.4: The soil moisture output of the SMIR algorithm using the T_B MRF after fifteen iterations. Comparing the results of the AVE iteration of SMIR using the T_B MRF, and the output after 15 iterations. In both images we can see a general loss in detail, and artifacts from the MRF appearing. This is likely due to the brightness temperature MRF being incompatible with the soil moisture measurements.

I note that the rSIR algorithm performs poorly at values close to zero. Because of this, I experimented by applying a linear transformation to the measurements in order to move the values away from zero during the rSIR iterations. After the rSIR iterations are completed, the inverse of the linear transform is applied. The transformation

$$SM(x,y)_{\text{trans}} = 10 * SM(x,y) + 100, \quad (5.2)$$

is used, where SM refers to a soil moisture estimate at a given pixel location. This modification does not provide any performance improvements by itself, and returns a very similar image to the un-transformed image output.

5.1.3 Soil Moisture Response Function Approach

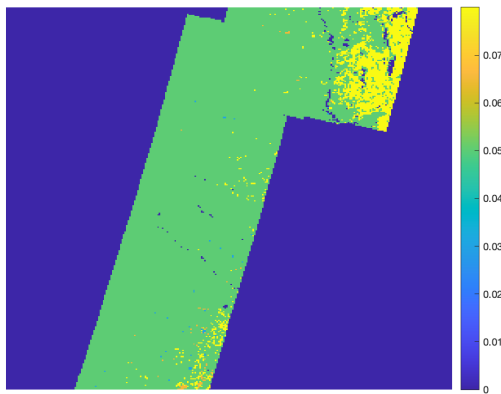
The motivation for deriving the soil moisture response function stems from the high resolution ancillary data available. Fig. 5.5 shows a collection of ancillary data for the area of interest. As illustrated in Fig. 5.5, there are many times when the ancillary data has a finer resolution than that of the brightness temperature measurements. By deriving a SMRF, the rSIR algorithm can be directly employed on soil moisture measurements that take into account as much of the high resolution ancillary data as possible. This begins by generating soil moisture measurements from the brightness temperature measurements.

5.1.4 Soil Moisture Footprint Derivation

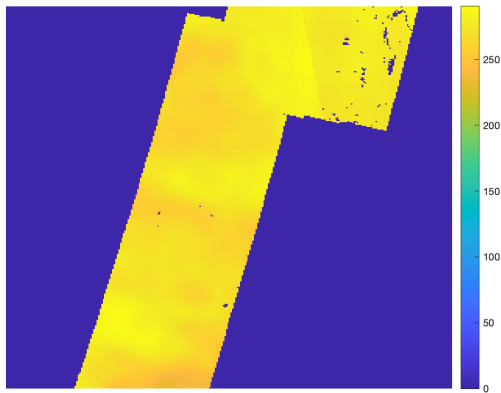
A soil moisture footprint is required to calculate the SMRF. The raw brightness temperature measurements are converted into soil moisture measurements. These brightness temperature measurements are the average brightness temperature over an entire radiometer footprint. The ancillary data is of a finer resolution than that of the brightness temperature measurements; the temporal coverage of the ancillary data can be more limited. However these temporally limited ancillary data sets can be assumed to be temporally stationary. When converting brightness temperature measurements to soil moisture measurements, only brightness temperature measurements that have all their corresponding ancillary data sets and overlap with the SMAP-SENTINEL-1 soil moisture product are used.

The next step is to calculate a brightness temperature footprint. This is done by multiplying the brightness temperature with the MRF,

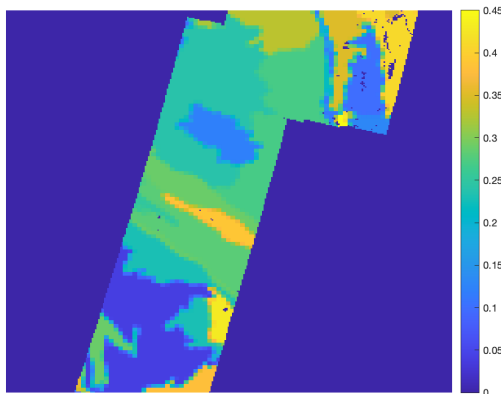
$$T_{B_{\text{Footprint}}}(i, j) = \frac{\text{MRF}(i, j)T_{B_{\text{Meas}}}}{\frac{1}{NM} \sum_i^M \sum_j^N \text{MRF}(i, j)}. \quad (5.3)$$



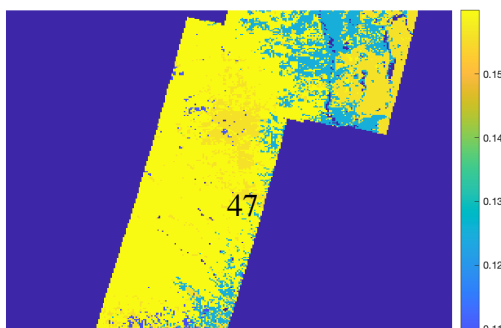
(a) Scattering Albedo



(b) Brightness Temperature



(c) Clay Fraction Index



Due to the limited dynamic range of the forward soil moisture transformation, the brightness temperature footprint is scaled. The scaling used is +/-10% about the mean of the MRF,

$$T_{B_{\text{Footprint}}} = \frac{1}{10}(T_{B_{\text{Footprint}}} - \mu_{T_{B_{\text{Footprint}}}}) + \mu_{T_{B_{\text{Footprint}}}}, \quad (5.4)$$

where $\mu_{T_{B_{\text{Footprint}}}}$ is the mean of the footprint. The scaled brightness temperature footprint is then transformed into a soil moisture footprint using the forward soil moisture transformation.

Nonzero Mean SMRF

Using the soil moisture footprint and the soil moisture measurement, the SMRF is calculated

$$\text{SMRF} = \frac{\text{SM}_{\text{Footprint}}}{\text{SM}_{\text{Meas}}}. \quad (5.5)$$

Two different methods are examined. The first uses this un-changed SMRF, and the second modifies the SMRF to be zero-mean. For both methods, by using the whole footprint much more of the high resolution ancillary data can be considered. This process produces a unique SMRF for each soil moisture measurement. The non-zero mean SMRF shares the same details and features as the zero mean SMRF. However, the two SMRFs produce outputs with stark differences.

The nonzero-mean SMRF is generally inversely proportional to the brightness temperature MRF. This means that values around the edge of the SMRF are weighted more than values at the center. An example of the nonzero-mean SMRF can be seen in Fig. 5.6. This SMRF is used to produce an AVE image as seen in Fig. 5.7. Overall, this SMRF shares many of the same attributes as the T_B MRF, resulting in an overall smooth image.

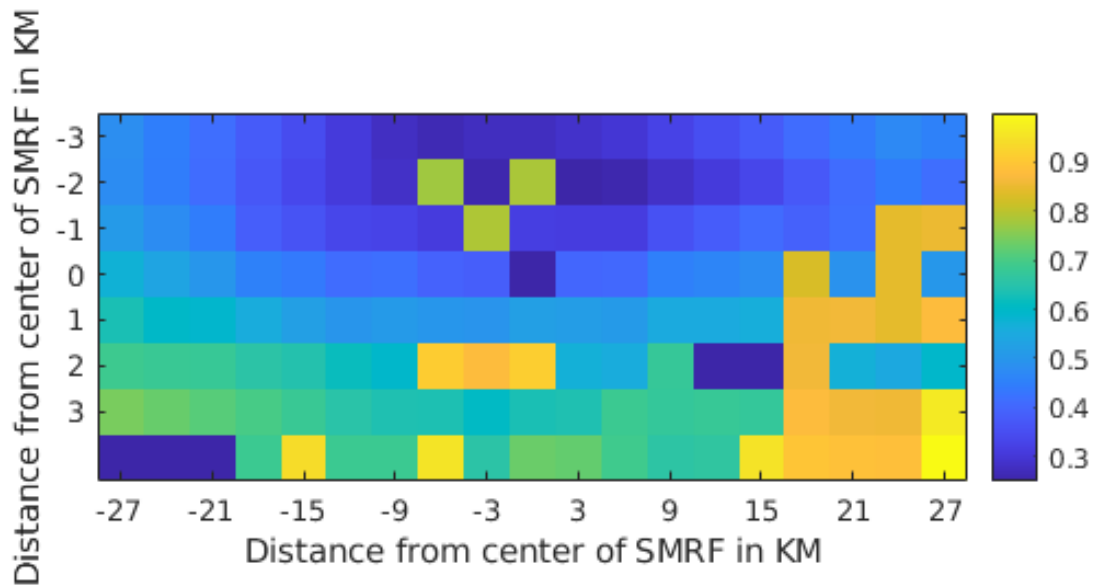


Figure 5.6: Example of a non-zero mean SMRF. The features are same as the zero mean SMRF. The main difference is the range of values. This particular SMRF is made over northern China using data from day 276 of 2016. The fine grained details in the SMRF arise from the fine details in the ancillary data. Each SMRF differs each other as the features in each footprint are different.

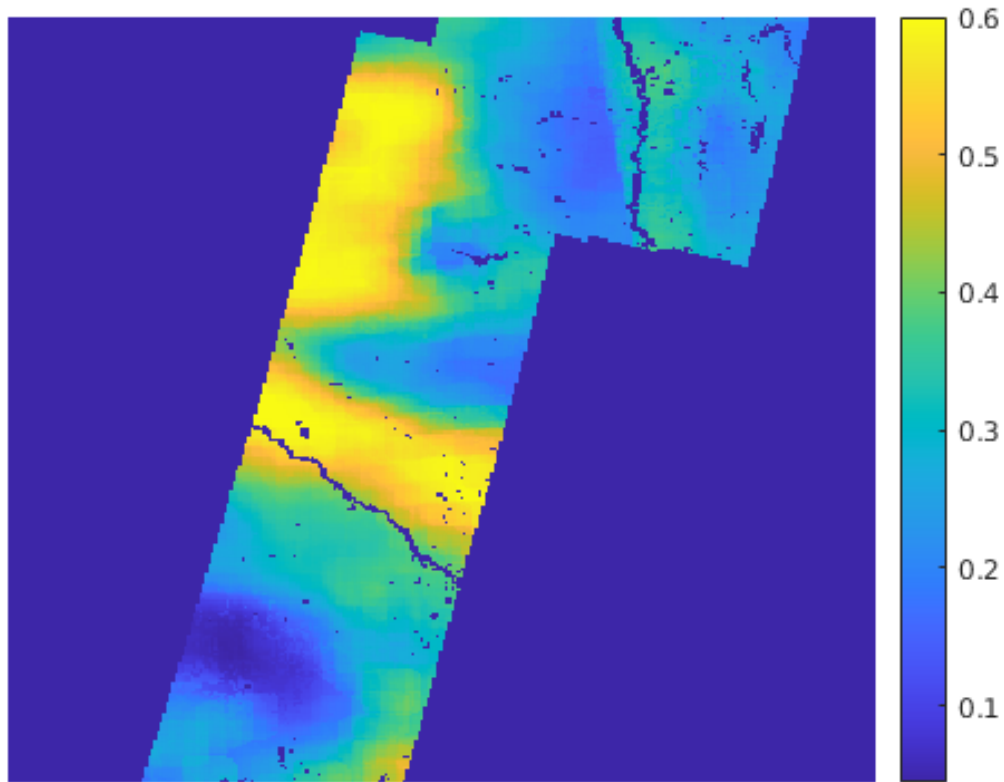


Figure 5.7: AVE image made using the non-zero SMRF. Note the general lack of detail, and features in the image. This image is produced using data from day 276 of 2016.

Zero-Mean SMRF

The zero-mean SMRF is made by simply subtracting the mean of each individual SMRF to produce a zero-mean SMRF

$$\text{SMRF}_{\text{zero}} = \text{SMRF} - \mu_{\text{SMRF}}, \quad (5.6)$$

where μ_{SMRF} is the mean of the soil moisture response function. An example of the zero-mean SMRF is shown in Fig. 5.8 and 5.9. This SMRF results in an AVE image with the finest detail but with inaccurate scaling. This can be seen in the existence of negative soil moisture estimates. Fig. 5.10 is an example of the AVE image produced using the zero-mean SMRF.

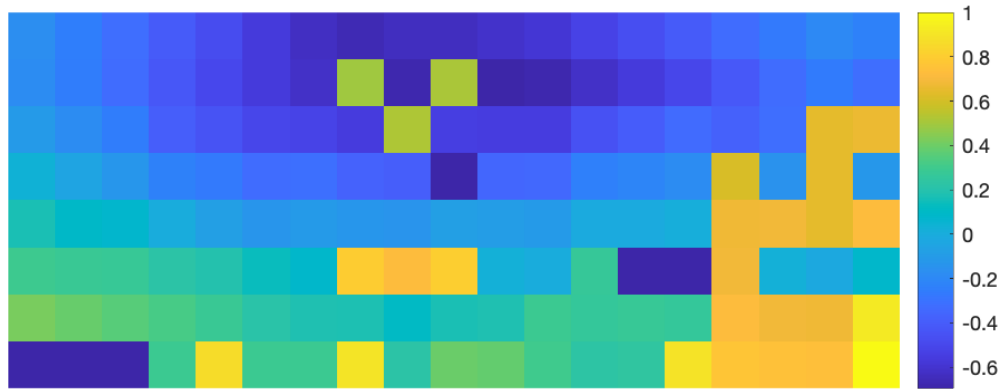


Figure 5.8: Example of a zero-mean SMRF made over Northern China. Made using data from day 276 of 2016. The fine grained details in the SMRF arise from the fine details in the ancillary data. Each SMRF differs each other as the features in each footprint are different.

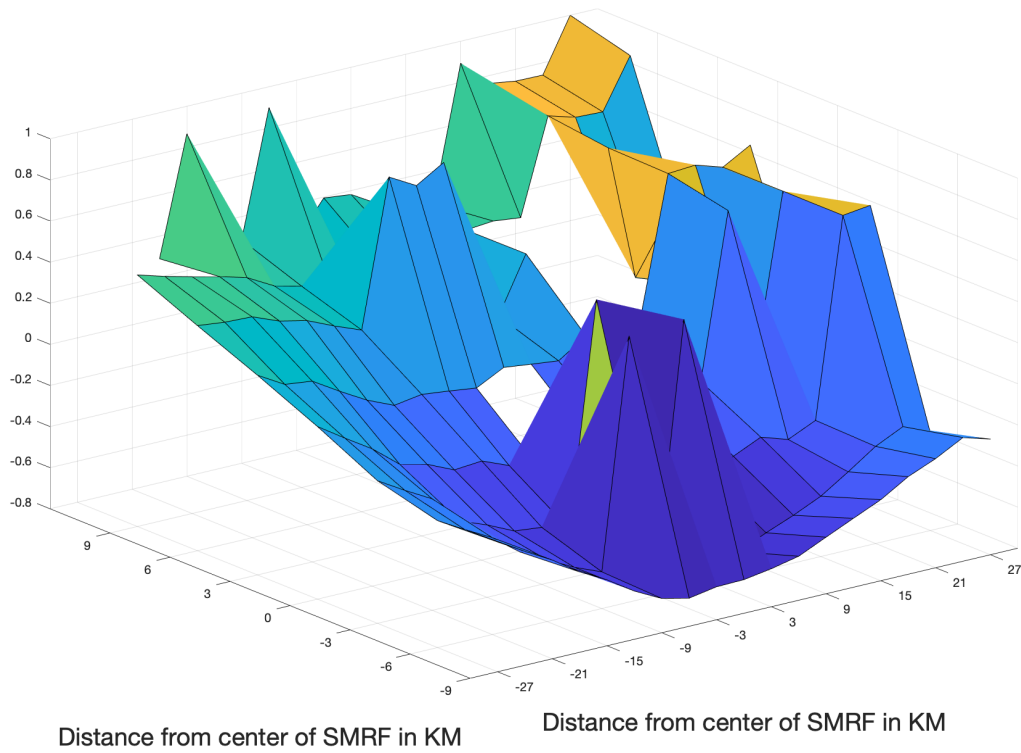


Figure 5.9: Surface plot of a zero mean SMRF. This figure shows the high resolution details as well as missing data pixels. The missing data pixels are caused by data missing in the ancillary data.

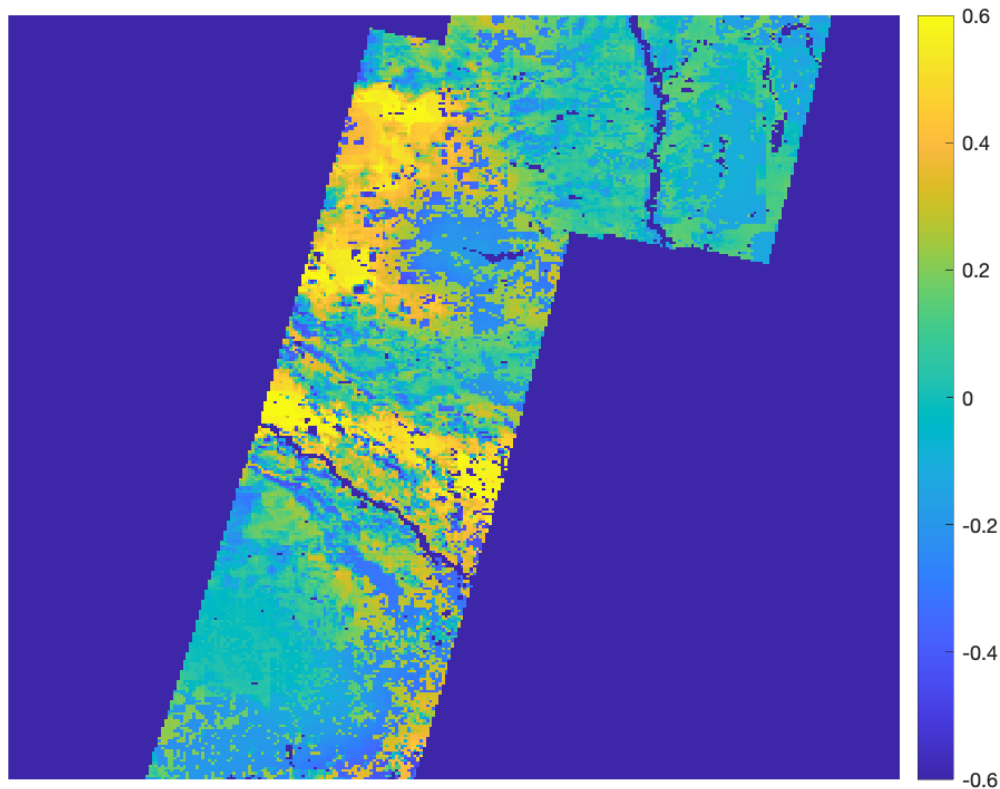


Figure 5.10: AVE image created using the zero mean SMRF. This image is centered over the Amazon river. Note the increase in detail and features in the image but also the negative values. Data is from day 276 of 2016.

The AVE image shown in Fig. 5.10 has much more detail than any other method examined so far. Also when compared with the sequential algorithm results, closely matches the existing features in the sequential image, but also shows other details not present. In Fig. 5.12 and Fig. 5.13 we can see rivers present in the SMIR that are not present in the SENINTEL-1 soil moisture estimate. To correct for the existence of negative values in this average image, the absolute value is taken. The results of this can be seen in Fig. 5.11. This operation produces an image that resembles the soil moisture image produced by JPL. This relationship shows that the negative values correspond to positive soil moisture measurements but require a different scaling. This implies that a transformation to the negative values in the SMRF could possibly produce accurate soil moisture estimates while retaining high detail.

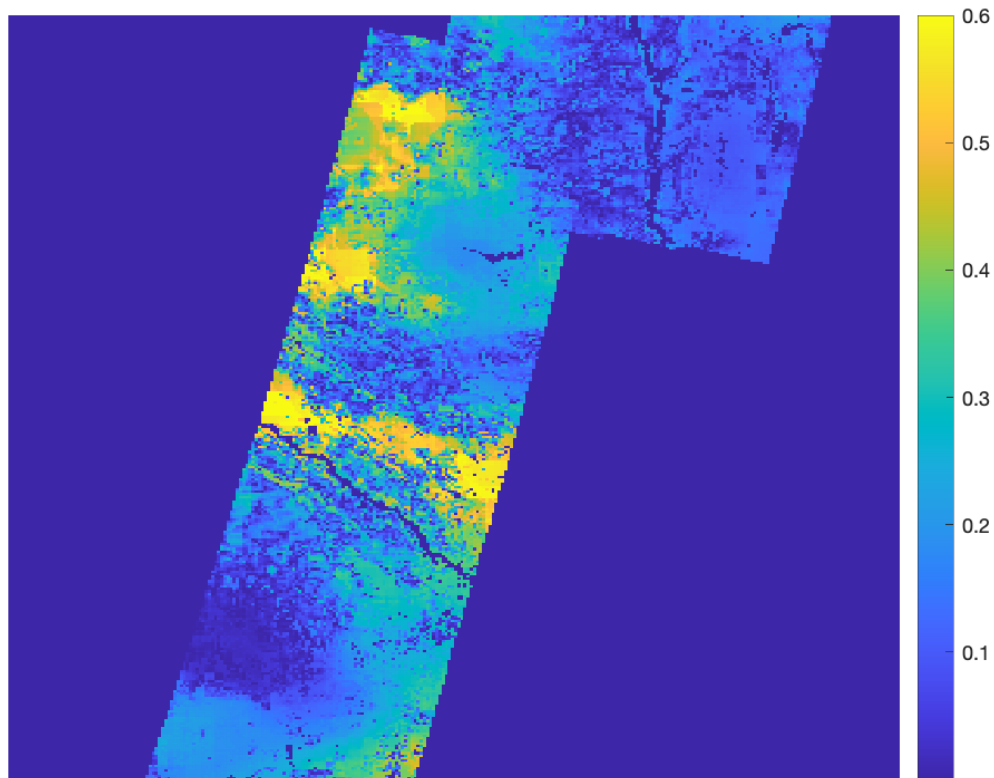


Figure 5.11: A corrected AVE image produced by taking the absolute value of the zero mean AVE image shown in Fig. 5.10. This image is made using data from day 276 of 2016.

Because the SMRF is centered about zero, a correction must be made so that it is compatible with the rSIR algorithm. The rSIR algorithm is a multiplicative algorithm. Because of this, measurements and MRFs with zeros can cause undefined behavior. The rSIR algorithm requires the measurements and MRF to be either strictly positive or strictly negative.

5.1.5 SMRF Corrections

This section addresses the zero-mean SMRF. In order to allow for rSIR processing multiple possible corrections to the zero-mean SMRF are postulated and their performance measured. The methods proposed focus on correcting the negative values of the SMRF. The rationale for this, is

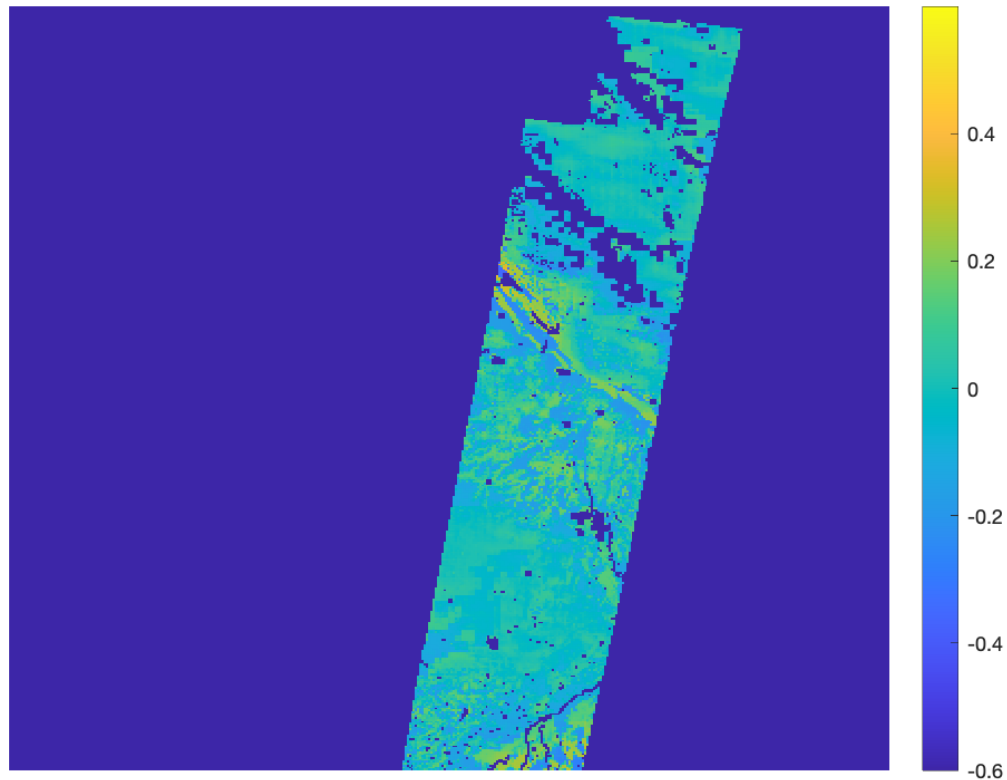


Figure 5.12: Example of features and details present in SMIR soil moisture estimate, but not present in the SENTINEL-1 soil moisture estimate. Compare with Fig. 5.13

the positive values in Fig. 5.10 are accurate when compared with the SENTINEL-1 soil moisture estimate.

Absolute Value of SMRF

The first method examined is calculating the absolute value of the SMRF. This allows the SMRF to be used in the combined rSIR algorithm and produces strictly positive soil moisture estimates. Fig. 5.14 shows the absolute value of the zero-mean SMRF. This correction is simply calculated as the absolute value of the SMRF with an added offset. The addition of the offset prevents division by zero errors from occurring.

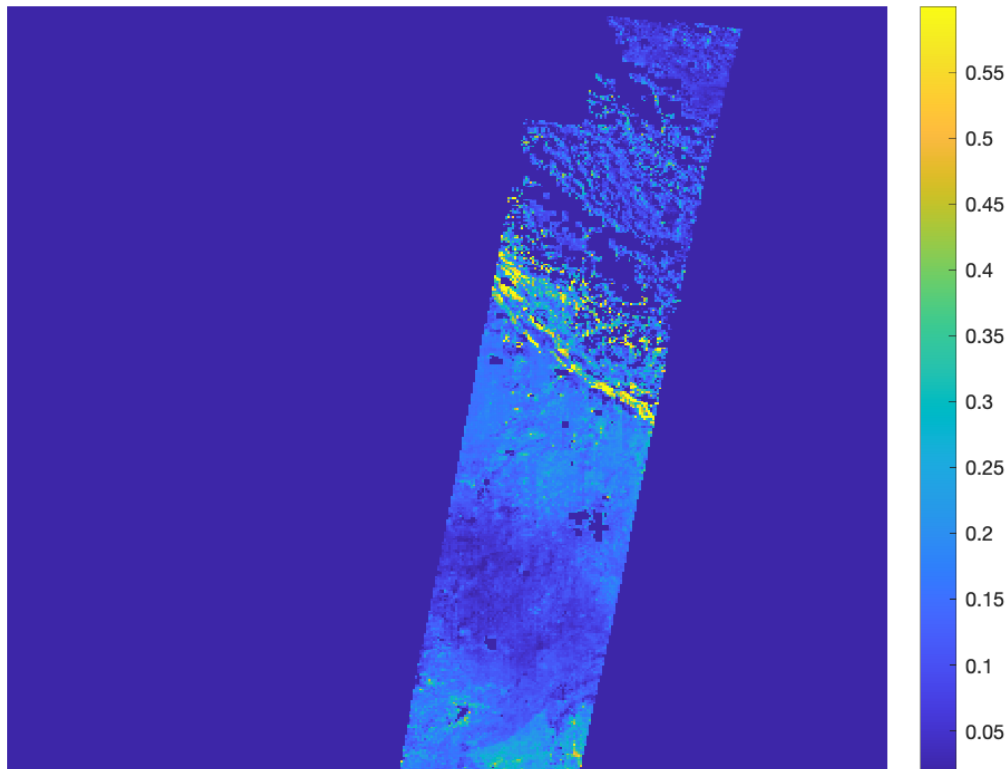


Figure 5.13: Example of features and details present in SMIR soil moisture estimate, but not present in the SENTINEL-1 soil moisture estimate. Compare with Fig. 5.12

$$SMRF_{abs} = |SMRF| + 0.01. \quad (5.7)$$

This correction results in mixed results. For some days of data, there is a loss of detail, and an increase in artifacts from the SMRF. This can be seen in Fig. 5.15. This correction allows for the rSIR reconstruction to be run directly using the $SMRF_{abs}$. For this day the rSIR algorithm slightly improves detail but also introduces artifacts, which are shown in Fig. 5.16. However, on other days, this correction performs very well. This can be seen in Fig. 5.17. Fig. 5.18 and Fig. 5.19 provide a more centered view of this area of both the absolute value SMRF correction, and the soil moisture estimate produced by JPL using both SMAP and SENTINEL-1 data. This provides an example of the absolute value SMRF correction performing well, and closely matching the JPL

estimate. On average, the absolute value of the SMRF matches the performance of the sequential algorithm (Table 5.1).

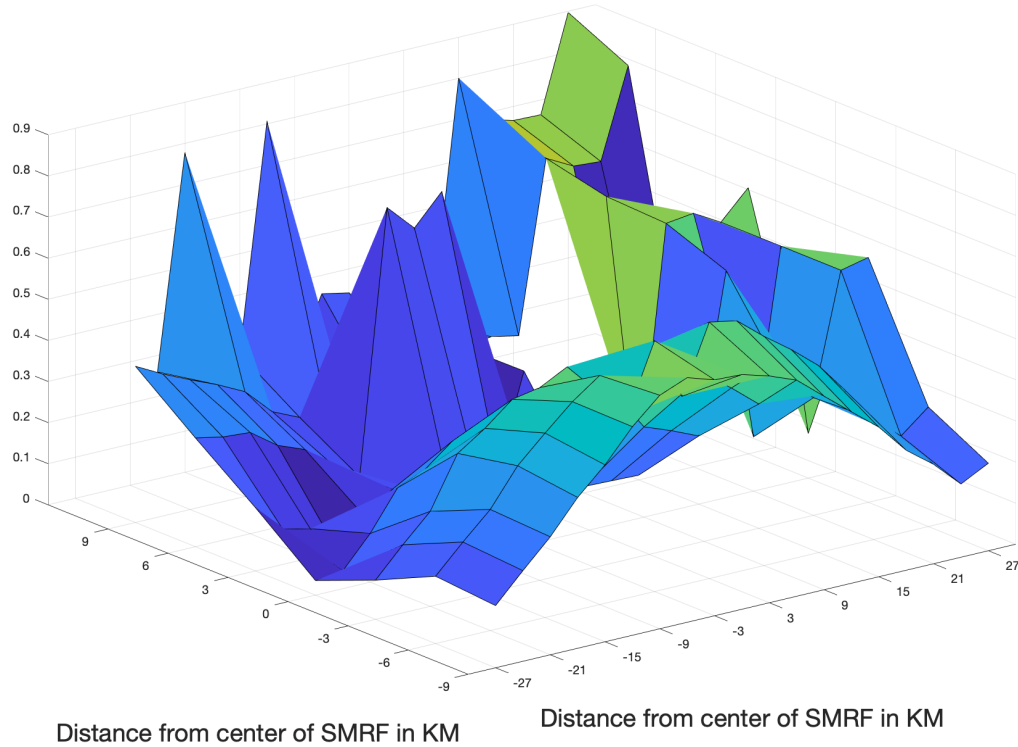


Figure 5.14: Absolute value of an example SMRF. This is made using the same data as in Fig. 5.9

Inverse of the SMRF

Another proposed method of correction of the SMRF is to use the inverse of the SMRF. As seen in the AVE images generated using the zero-mean SMRF, the negative values may correspond to weighted, positive counterparts. This method is calculated to determine if there is any validity to this claim. This transformation on the SMRF is given as,

$$\text{SMRF} = \begin{cases} \left| \frac{1}{\text{SMRF}} \right| & \text{SMRF} < 0 \\ \text{SMRF} & 0 \leq \text{SMRF}. \end{cases}$$

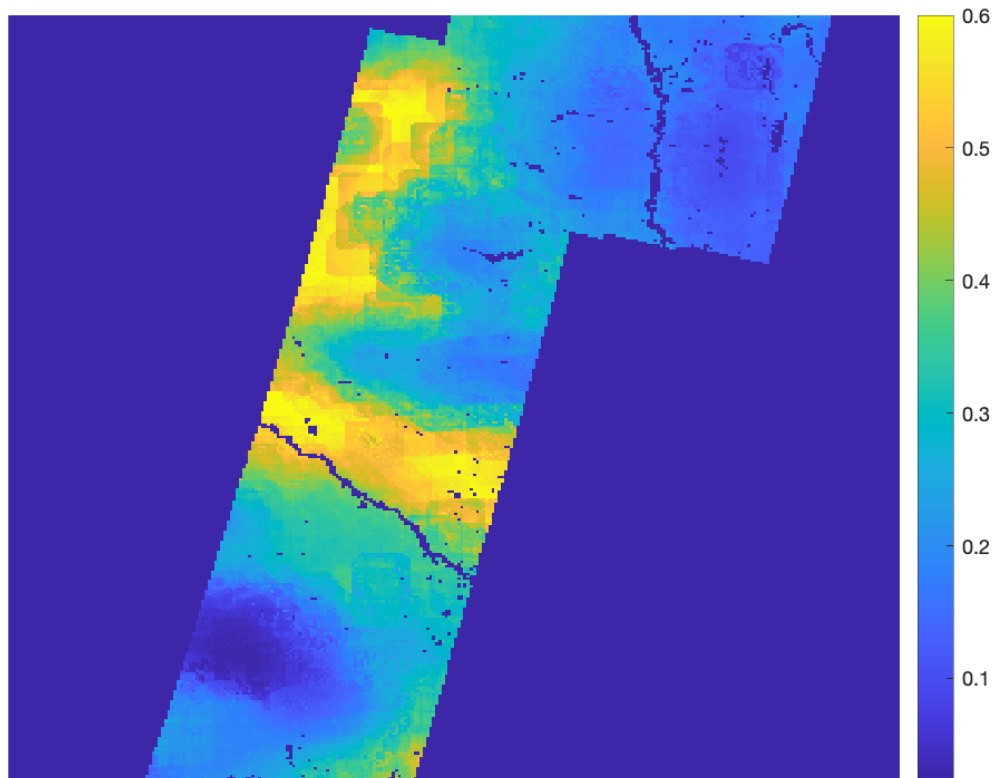


Figure 5.15: Resulting AVE image using the absolute value of the SMRF. It is important to note the general loss in detail in the image. Made using data from day 276 of 2016.

This produces an AVE image (Fig. 5.20) that performs better than any of the other previous methods, and retains much finer detail. The benefit of this approach is that the rSIR algorithm can be run on this image to improve the results. The results of the rSIR algorithm can be seen in Fig. 5.21.

After running the rSIR algorithm for fifteen iterations, we can see an increase in both detail and artifacts from the SMRF. The artifacts can be seen in the areas with high soil moisture. This is considered a minor issue because the measurements for these areas can be unreliable and are usually clipped. On average, this approach is capable of out performing the sequential algorithm. This can be seen in Table 5.1.

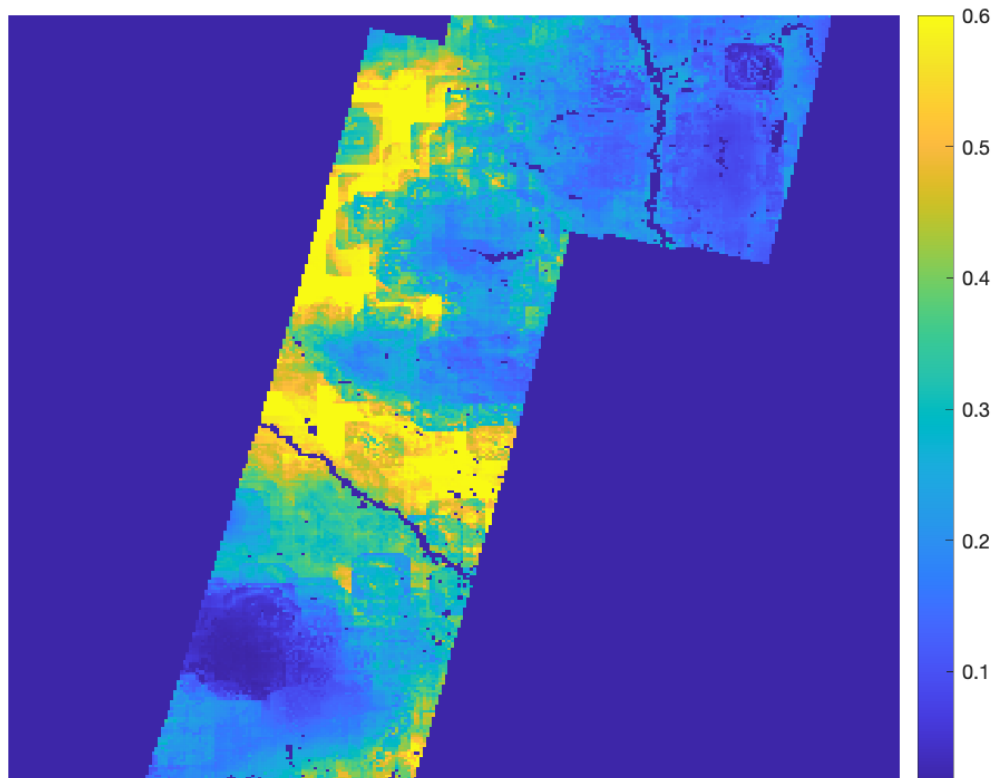


Figure 5.16: Result of the absolute value SMRF after fifteen iterations of the combined rSIR algorithm. Made using data from day 276 of 2016.

Negative Lobe SMRF

The Negative Lobe SMRF is made by discarding all the positive values of the zero-mean SMRF. This strictly negative SMRF produces a negative soil moisture estimate. To remedy this, the absolute value of the SMRF is taken. This method produces a good image with few artifacts from the processing. The AVE image is shown in Fig. 5.22. This image retains a higher amount of detail when compared with other methods examined thus far. However, by discarding the positive values, some detail is lost. Similar to the inverse SMRF technique, these areas with high soil moisture are unstable and are usually clipped. This method's strength is seen once the rSIR algorithm is applied. The rSIR algorithm increases the detail of the image with less noise amplification and artifacting when compared with all previous methods examined thus far. Fig. 5.23 shows the

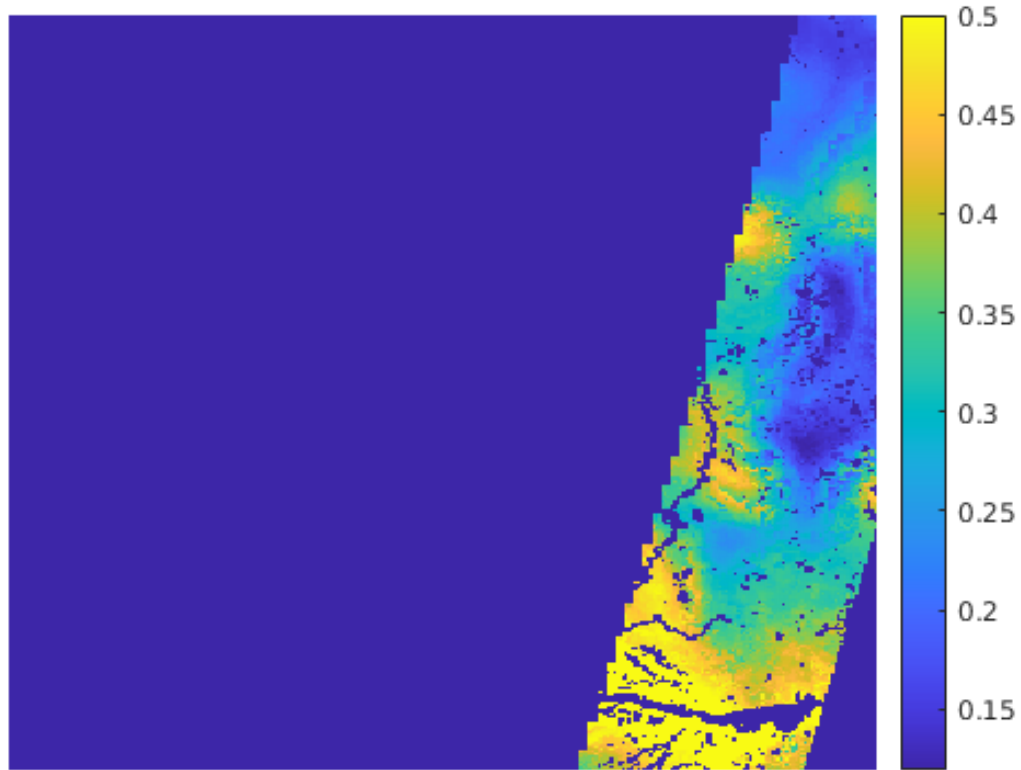


Figure 5.17: Soil moisture estimate from day 280 of 2016. This image is made using the $SMRF_{abs}$. This image is taken from the same area of study as outlined in Fig 4.1

results of the rSIR algorithm using the negative lobe of the SMRF. Again, this approach is capable of outperforming the sequential algorithm. This can be seen in Table 5.1.

$$SMRF = \begin{cases} |SMRF| & SMRF < 0 \\ 0 & 0 \leq SMRF. \end{cases} \quad (5.8)$$

5.2 Analysis

Adapting rSIR to calculate its update in soil moisture space does not perform as well as hoped when using the brightness temperature measurement response function (MRF). The method

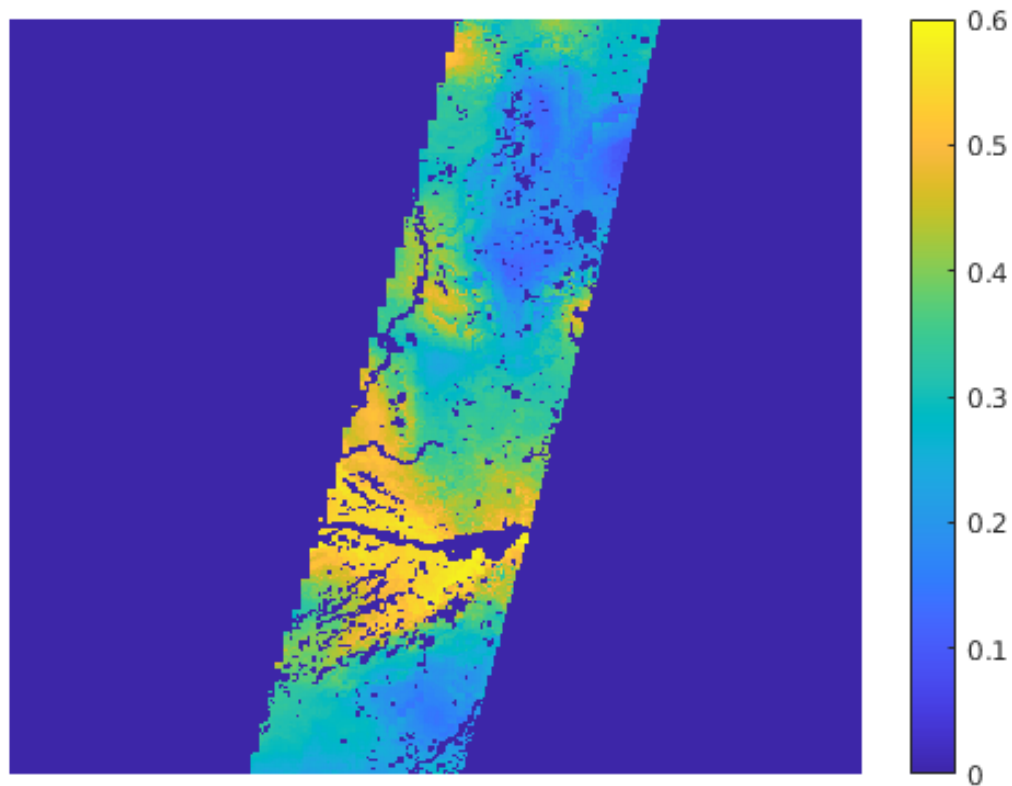


Figure 5.18: A more centered view of the area from Fig 5.17. This is again data from day 280 of 2016. When compared with Fig 5.19, we can see that much of the details and features are present.

produces results lacking detail. This result encourages the derivation of a soil moisture response function that can utilize all the information in the ancillary data during the rSIR iterations.

The SMRF itself does not improve the soil moisture estimates made by rSIR. This method exhibits all the same attributes as using the brightness temperature MRF and converges to roughly the same low resolution solution. Improvements are only made when transformations are performed on the SMRF. The SMRF resolves finer details when centered about zero.

When the SMRF is zero-mean and allowed to contain positive and negative values, it can allow for more detail to be resolved in soil moisture estimates at the cost of the scale accuracy. This can be corrected in the image product, allowing for a remarkably detailed average image. However, this zero-mean SMRF is incompatible with the rSIR algorithm. Transformations to create an all positive SMRF ultimately degrades the amount of detail in the soil moisture estimation. This

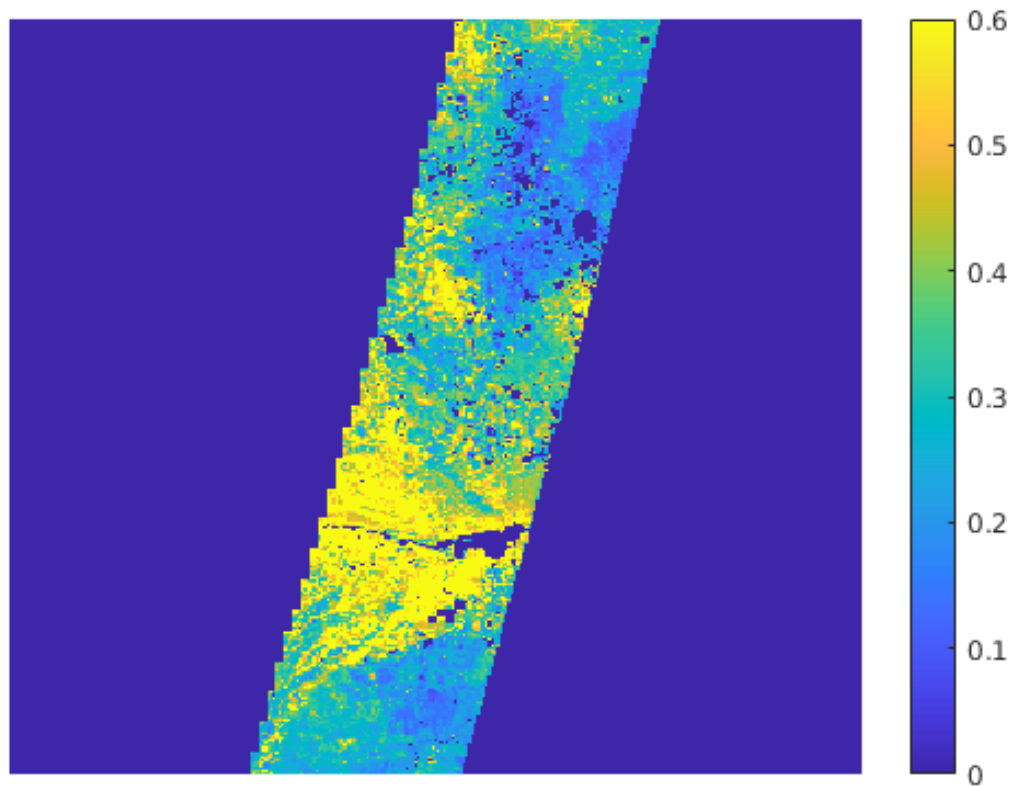


Figure 5.19: A soil moisture estimate produced by JPL using SMAP and SENTINEL-1 measurements. This is made using data from day 280. This view is identical to that of Fig. 5.18 for comparison.

dynamic is difficult to explain as an offset to the SMRF should not effect the resulting image as much as it does. Further, this property does not show up in the simulations. I believe that the negative values of the SMRF can be mapped to positive values using a positive function. However, I was unable to derive what this function should be. Using ad-hoc approaches, retaining only the negative lobe of the SMRF produced the most desirable images. However, the three corrections analyzed in this thesis all performed well, either matching or slightly outperforming the sequential algorithm.

Currently, the AVE image constructed using the zero-mean SMRF outperforms any rSIR approach and closely matches the soil moisture data product currently being produced by the NASA JPL. And in some cases, it resolves details that are expected but not present in the JPL

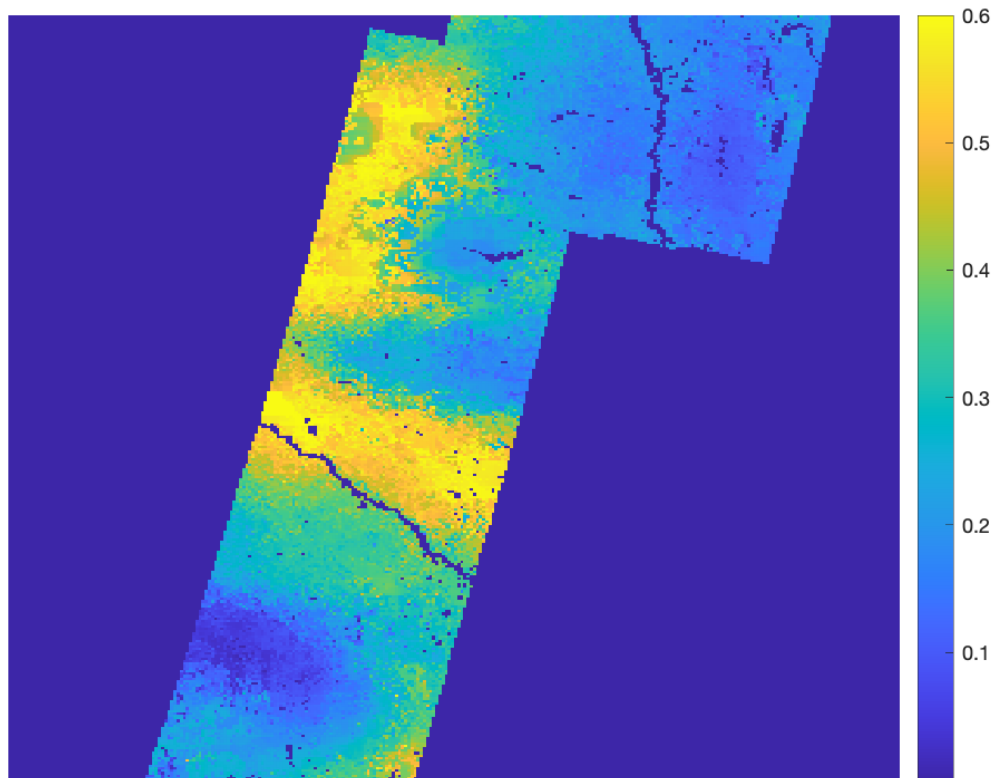


Figure 5.20: AVE image produces using the inverse of the SMRF. This AVE image retains much more detail compared to the other methods proposed.

soil moisture data product. This is most visible in the existence of the river in the top right of the sample average images using the zero-mean SMRF and the lack of the same river in the JPL soil moisture data product.

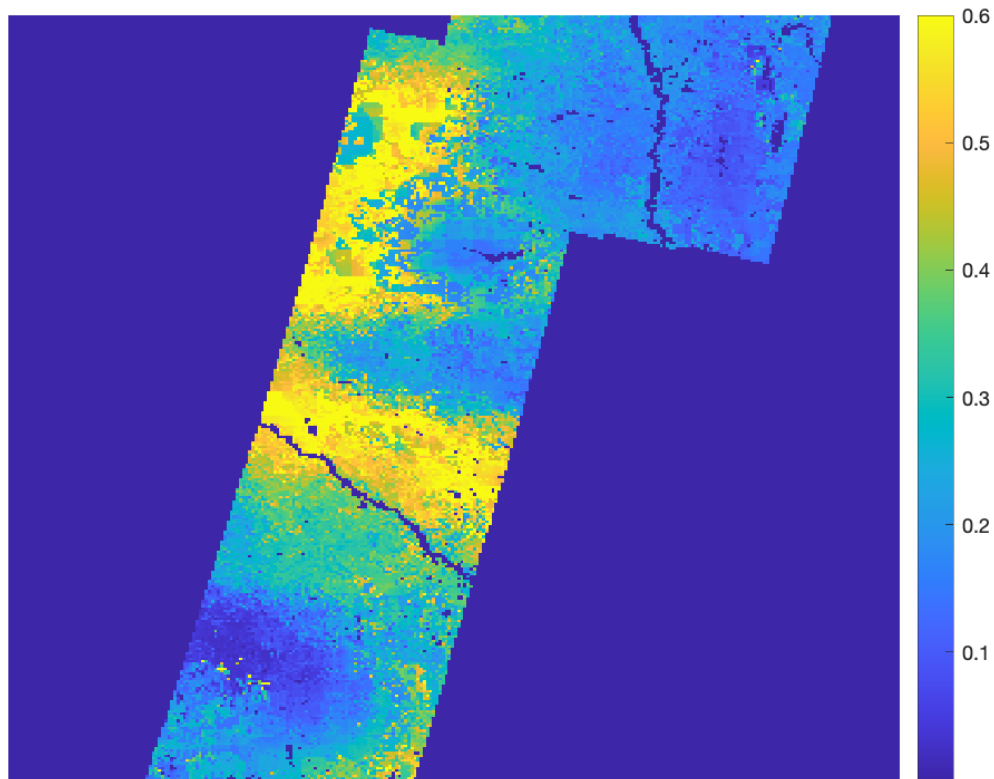


Figure 5.21: SIR image produced after fifteen iterations using the inverse of the SMRF.

Table 5.1: Table of errors that have been averaged over a 7-day window. These errors are calculated as the difference between the SENTINEL-1 soil moisture estimate and the SMIR soil moisture estimate. These errors are averaged from day 276-282 of 2016. These errors are calculated after performing the rSIR reconstruction on using the various SMRF corrections. The reconstruction is run until the error begins to increase and then is stopped. Depending on the day the number of iterations range from 15-40.

Method	Total Mean Error	Root Mean Squared Error
Sequential	0.0537	0.0916
Absolute Value SMRF	0.0542	0.0827
SMIR Inverse SMRF	0.0456	0.0687
SMIR Negative Lobe	0.0453	0.0689

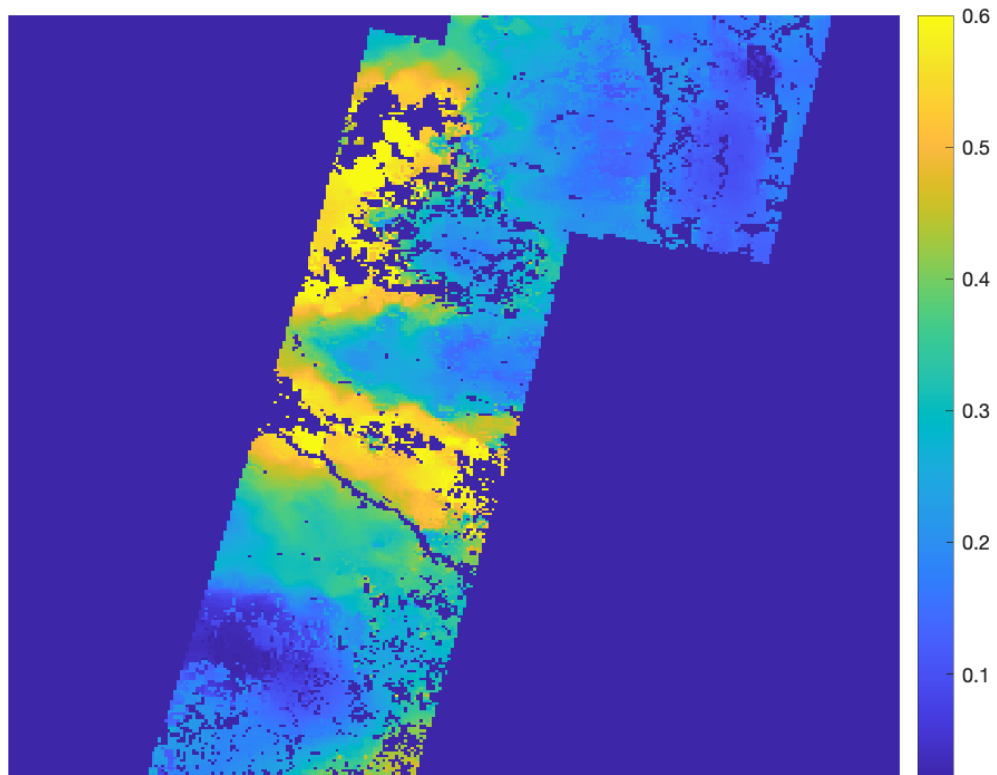


Figure 5.22: Average produced using the Negative Lobe of the SMRF. This image is made using data from day 276 of 2016.

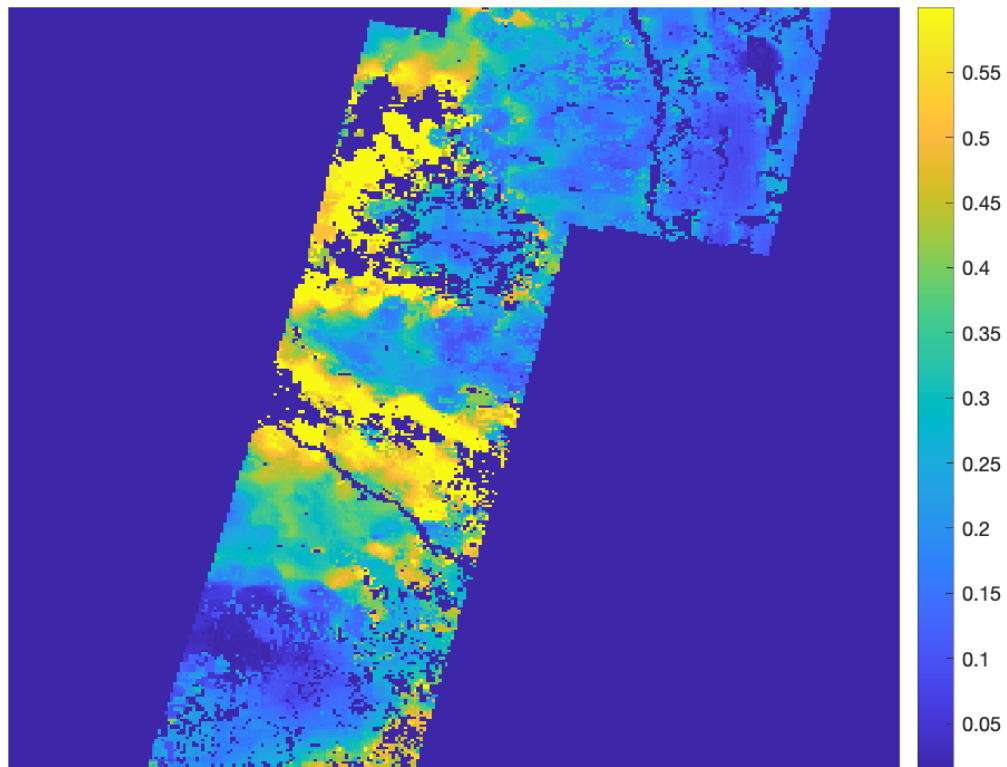


Figure 5.23: SMIR image produced after 15 iterations using the negative lobe of the SMRF. This image is produced using data from day 276 of 2016.

CHAPTER 6. CONCLUSION

This thesis explores various methods for improving the high resolution soil moisture measurements produced by the SMAP sensor. It focuses on exploring various techniques on combining the rSIR and soil moisture algorithms in order to achieve this goal. Two main approaches are considered: calculating the iterative update in brightness temperature, and calculating the update in soil moisture. These two methods had varying results, neither of which ultimately perform up to the standard of sequentially performing the rSIR algorithm followed by the forward soil moisture transformation.

The approach where the rSIR iterative update is calculated in brightness temperature provides performance increase and produces images with limited detail. While the estimates are accurate, it ultimately is not a significant improvement over the sequential method.

When considering the approach where the rSIR iterative update is calculated in soil moisture, two main approaches are considered. The first is using brightness temperature measurement response function (MRF), and the second is using a soil moisture response function (SMRF). When the brightness temperature MRF is used, the results are accurate but lack detail and precision. This is because much of the high resolution ancillary data is discarded. This method ultimately does not provide any performance improvement over the sequential method.

Using a SMRF provided various levels of performance depending on the SMRF used. When the SMRF was strictly positive with a non-zero mean, the performance of the algorithm is approximately the same as using the brightness temperature MRF. However, by using a zero-mean SMRF, the rSIR algorithm is able to produce very detailed average images at the expensive of accuracy. Various corrections to the SMRF are proposed and benchmarked. The three corrections proposed in this thesis perform well, either matching or outperforming the sequential algorithm on average.

6.1 Contributions

This thesis makes the following contributions to SMAP processing:

- Explored variations of the rSIR algorithm to enable high resolution soil moisture image reconstruction.

Examined two main variations on the rSIR algorithm: the SMrSIR, and the SMIR algorithms. While the disaggregation algorithm currently employed by JPL provides accurate soil moisture estimates, it is constrained to a narrow overlap between the SMAP and SENTINEL-1 swath. Using upsampling techniques that are not reliant on higher resolution measurements enables soil estimates to be made using the entire SMAP swath. This thesis examines two new methods for producing high resolution soil moisture estimates over the entire SMAP swath.

- Derived and designed a novel SMrSIR algorithm to enable high resolution soil moisture image reconstruction over the entire SMAP swath.

The SMrSIR algorithm is a variation of the rSIR algorithm and soil moisture algorithm that combines the two algorithms into a single reconstruction algorithm. The SMrSIR is characterized by the iterative update calculation taking place in the brightness temperature space. This method calculates accurate results, but the implementation examined in this thesis does not provide a significant performance improvement.

- Derived and designed a novel SMIR algorithm to enable high resolution soil moisture image reconstruction over the entire SMAP swath.

The SMIR algorithm is a variation of the rSIR algorithm and soil moisture algorithm that combines the two algorithms into a single reconstruction algorithm. The SMIR algorithm is characterized by the iterative update being calculated in soil moisture space. The SMIR algorithm performs best when a soil moisture response function (SMIRF) is used. This thesis examines multiple possible SMRFs that could be used.

- Derived multiple possible SMRFs to be used in the SMIR algorithm.

The SMRF serves as a replacement to the measurement response function (MRF) used in brightness temperature image reconstruction. While the MRF is derived from the antenna

gain pattern, the SMRF is derived from ancillary data sets. This allows for a greater amount of detail to be resolved as many of the ancillary data sets have a greater spatial resolution than the brightness temperature measurements.

6.2 Future Work

There are aspects of this thesis that could be extended upon as future work. Suggestions for future work are:

- Further explore the SMRF. The SMRF produced in this thesis works well but could be improved upon. The zero-mean SMRF can likely be transformed into a strictly positive or strictly negative SMRF that can be more compatible with the rSIR algorithm. The SMRF allows for a great deal of detail to be resolved in the soil moisture estimate.
- Adapt rSIR to allow for both positive and negative values. The rSIR algorithm is a multiplicative algorithm and values that are zero cause division by zero errors. The rSIR algorithm could be adapted to solve the positive and negative values separately and merge the results at the end.
- Further explore other brightness temperature up-sampling algorithms to improve soil moisture estimates. The rSIR algorithm is not the only algorithm that can be used to increase the brightness temperature measurements. For example, the Backus-Gilbert inversion can be used in place of the rSIR algorithm.
- This study suggests that we can produce high resolution soil moisture estimates from only radiometer measurements. These results should be validated against in-situ soil moisture measurements.

REFERENCES

- [1] D. Entekhabi, S. Yueh, P. E. O’Neill, and K. H. Kellogg, *SMAP Handbook*. NASA JPL, 2014. vii, 2, 3, 8, 9, 10
- [2] JPL, “SMAP L1C S0 HiRes V3 Dataset,” Internet, 10 2016. [Online]. Available: <https://nsidc.org/data/SPL3SMA/versions/3> vii, viii, 11, 42
- [3] J. C. Hill and D. G. Long, “Extension of the QuikSCAT Sea Ice Extent Data Set With OSCAT Data,” *IEEE Geoscience and Remote Sensing Letters*, vol. 14, no. 1, pp. 92–96, 2017. 1
- [4] R. West, “Soil Moisture Active and Passive Mission ATBD,” Internet, April 2014. [Online]. Available: <https://smap.jpl.nasa.gov/documents/> 1, 2, 7
- [5] B. R. Hicks and D. G. Long, “Inferring Greenland melt and refreeze severity from SeaWinds scatterometer data,” *International Journal of Remote Sensing*, vol. 32, no. 23, pp. 8053–8080, 2011. [Online]. Available: <https://doi.org/10.1080/01431161.2010.532174> 1
- [6] F. T. Ulaby and D. G. Long, *Microwave Radar and Radiometric Remote Sensing*, 1st ed. University of Michigan Press, 2013. 1, 2, 15, 37
- [7] P. O’Neill, R. Bindlish, S. Chan, J. Chaubell, E. Njoku, and T. Jackson, “Algorithm Theoretical Basis Document Level 2 3 Soil Moisture (Passive) Data Products,” Internet, 11 2020. [Online]. Available: <https://smap.jpl.nasa.gov/documents/> 1, 10, 13
- [8] “Proximate Cause of the SMAP Radar Failure,” 03 2019, press Release describing hardware failure. 1, 2, 7
- [9] T. Gallagher and W. Cooke, “Interactions of blackbody radiation with atoms,” *Physical Review Letters*, vol. 42, no. 13, p. 835, 1979. 1
- [10] J. Brown, “An Exploration of Neural Networks in Enhanced Resolution Remote Sensing Products,” Master of Science, Brigham Young University, 2019. 2, 3, 14
- [11] D. G. Long, M. J. Brodzik, and M. A. Hardman, “Enhanced-Resolution SMAP Brightness Temperature Image Products,” *IEEE Transactions on Geoscience and Remote Sensing*, vol. 57, no. 7, pp. 4151–4163, 2019. 7, 19, 20
- [12] D. Entekhabi, E. G. Njoku, P. E. O’Neill, K. H. Kellogg, W. T. Crow, W. N. Edelstein, J. K. Entin, S. D. Goodman, T. J. Jackson, J. Johnson, J. Kimball, J. R. Piepmeier, R. D. Koster, N. Martin, K. C. McDonald, M. Moghaddam, S. Moran, R. Reichle, J. C. Shi, M. W. Spencer, S. W. Thurman, L. Tsang, and J. Van Zyl, “The Soil Moisture Active Passive (SMAP) Mission,” *Proceedings of the IEEE*, vol. 98, no. 5, pp. 704–716, 2010. 7
- [13] “Specifications.” [Online]. Available: <https://smap.jpl.nasa.gov/observatory/specifications/> 9

- [14] P. O’Neill, R. Bindlish, S. Chan, J. Chaubell, E. Njoku, and T. Jackson, “Algorithm Theoretical Basis Document Level 2 3 Soil Moisture (Passive) Data Products,” Internet, 11 2014. [Online]. Available: <https://smap.jpl.nasa.gov/documents/> 10
- [15] *SENTINEL-1 Technical Guide*. ESA, April 2014. [Online]. Available: <https://sentinels.copernicus.eu/web/sentinel/technical-guides/sentinel-1-sar> 10
- [16] P. O’Neill, R. Bindlish, S. Chan, J. Chaubell, E. Njoku, and T. Jackson, “Algorithm Theoretical Basis Document L2 L3 Radar/Radiometer Soil Moisture (Active/Passive) Data Products,” Internet, 11 2014. [Online]. Available: <https://smap.jpl.nasa.gov/documents/> 12
- [17] J. Peng, P. Mohammed, J. Chaubell, S. Chan, S. Kim, N. Das, S. Dunbar, R. Bindlish, and X. Xu, “Soil Moisture Active Passive (SMAP) L1-L3 Ancillary Static Data, Version 1,” Internet, 2019. [Online]. Available: https://nsidc.org/data/SMAP_L1_L3_ANC_STATIC/versions/1 12
- [18] M. C. Dobson, F. T. Ulaby, M. T. Hallikainen, and M. A. El-rayes, “Microwave Dielectric Behavior of Wet Soil-Part II: Dielectric Mixing Models,” *IEEE Transactions on Geoscience and Remote Sensing*, vol. GE-23, no. 1, pp. 35–46, 1985. 15
- [19] O. Calla, D. Bohra, R. Vyas, B. S. Purohit, R. Prasher, A. Loomba, and N. Kumar, “Measurement of soil moisture using microwave radiometer,” in *2008 International Conference on Recent Advances in Microwave Theory and Applications*, 2008, pp. 621–624. 15
- [20] D. Early and D. Long, “Image reconstruction and enhanced resolution imaging from irregular samples,” *IEEE Transactions on Geoscience and Remote Sensing*, vol. 39, no. 2, pp. 291–302, 2001. 17
- [21] D. Long and M. Brodzik, “Optimum Image Formation for Spaceborne Microwave Radiometer Products,” *IEEE Transactions on Geoscience and Remote Sensing*, vol. 54, pp. 1–17, 12 2015. 24, 41
- [22] M. J. Brodzik, B. Billingsley, T. Haran, B. Raup, and M. H. Savoie, “EASE-Grid 2.0: Incremental but Significant Improvements for Earth-Gridded Data Sets,” 2012. [Online]. Available: <http://www.mdpi.com/2220-9964/1/1/32> 25